Evaluation of radiative depolarization in the future circular electron-positron collider

Wenhao Xia,[1,2,3] Zhe Duan,[1,*] Desmond P. Barber,[4,5] Yiwei Wang,[1] Bin Wang,[1] and Jie Gao[1,2,†]

[1]*Key Laboratory of Particle Acceleration Physics and Technology, Institute of High Energy Physics,*
Chinese Academy of Sciences, 19B Yuquan Road, Beijing 10049, China
[2]*University of Chinese Academy of Sciences, 19A Yuquan Road, Beijing 10049, China*
[3]*State Key Laboratory of NBC Protection for Civilians, Beijing 102205, China*
[4]*Deutsches Elektronen-Synchrotron DESY, Notkestraße 85, 22607 Hamburg, Germany*
[5]*Department of Mathematics and Statistics, University of New Mexico,*
Albuquerque, New Mexico 87131, USA

(Received 18 January 2023; accepted 1 June 2023; published 12 September 2023)

Spin-polarized lepton beams are an important aspect in the design of the future 100-km scale Circular Electron Positron Collider (CEPC). Precision beam energy calibration using resonant depolarization, as well as longitudinally polarized colliding beams, is being actively investigated. The attainable beam polarization level for various beam energies and application scenarios depends on the radiative depolarization in the collider rings. In this paper, the radiative depolarization effects are evaluated for a CEPC collider ring lattice with detailed machine imperfections and corrections. Simulations with the SLIM and Monte Carlo approaches using the Bmad/PTC codes are compared with the theory of the effects of spin diffusion for ultrahigh beam energies and the validity of the theories, with special attention to that of so-called uncorrelated resonance crossing, is thereby addressed.

DOI: 10.1103/PhysRevAccelBeams.26.091001

I. INTRODUCTION

After the discovery of the Higgs particle at the Large Hadron Collider (LHC), a study of the Circular Electron Positron Collider (CEPC) was launched as one of the global design efforts of future electron-positron circular colliders [1,2], for precision measurements of Higgs boson properties and electroweak interactions, as well as direct searches for new physics with unprecedented accuracy. In the conceptual design report (CDR) [3] released in November 2018, the CEPC was designed as a double-ring collider with a circumference of about 100 km and to be operated at beam energies of around 45 GeV as a Z factory, 80 GeV as a W factory, and 120 GeV as a Higgs factory ($e^+e^- \to ZH$). After the CDR, the CEPC accelerator entered the phase of the technical design report (TDR) endorsed by the CEPC International Advisory Committee (IAC). Recent updates of the CEPC accelerator R&D are summarized in [4].

Beam polarization is an important design aspect of the CEPC. On one hand, the resonant depolarization (RD) technology [5] is essential for precision beam energy calibration at the Z-pole and the WW threshold. RD utilizes a horizontal oscillating magnetic field to excite a vertically polarized beam. As the excitation frequency is scanned, the beam gets depolarized when the perturbation is resonant with the spin precession frequency, which is closely related to the beam energy. RD requires a vertical beam polarization level of 5%–10% at the CEPC, according to experience at LEP [6]. On the other hand, colliding beam experiments with longitudinal beam polarization, which would greatly broaden the potential of the physics program, are also being explored at the CEPC [7]. For this purpose, a longitudinal beam polarization of at least 50% for one or both e^+ and e^- beams at the interaction points is desired. These require preparation and maintenance and then manipulation of the polarized e^+/e^- beams with spin rotators.

Spin rotators have been successfully included in the CEPC CDR lattice for the Z-pole energy in a separate study [8]. Note that since the e^+ and e^- beams in the CEPC are in separate rings, their spin helicities can be controlled independently. In addition, a separate study [9] has investigated the depolarization during the acceleration process in the booster synchrotron showing that the highly periodic lattice features generally weak spin resonances and that the beam polarization is well maintained in the acceleration up to 80 GeV.

The precession of the spin expectation value $\vec{S}$, and of $\hat{S} = \vec{S}/|\vec{S}|$, of a relativistic charged particle, in electric and magnetic fields follows the Thomas-BMT equation [10,11],

---

[*] duanz@ihep.ac.cn
[†] gaoj@ihep.ac.cn

which, for a circular accelerator or storage ring, can be expressed in the following form:

$$\frac{d\hat{S}}{d\theta} = [\vec{\Omega}_0(\theta) + \vec{\omega}(\vec{u};\theta)] \times \hat{S}. \tag{1}$$

with

$$\vec{\Omega}_0(\theta) = \vec{\Omega}_{00}(\theta) + \Delta\vec{\Omega}(\theta), \tag{2}$$

where $\vec{\Omega}_0(\theta)$ is the spin-precession vector on the closed orbit at the azimuthal angle θ. $\vec{\Omega}_{00}(\theta)$ and $\Delta\vec{\Omega}(\theta)$ denote the contribution of the fields on the design orbit and the magnet errors/correction fields to the spin precession vector, respectively. $\vec{\omega}(\vec{u};\theta)$ is due to the orbital oscillations $\vec{u}$ relative to the closed orbit. We use a Frenet-Serret coordinate system, where $\vec{e}_x, \vec{e}_y, \vec{e}_z$ are the unit vectors pointing radially outwards, vertically upwards, and longitudinally (clockwise), respectively, so that they form a right-handed unit-vector basis. In this coordinate system, the particle's phase-space coordinates can be expressed as $\vec{u} = (x, p_x, y, p_y, z, \delta)$. x and y are the transverse coordinates of the particle. The transverse phase-space momenta P_x and P_y are normalized by the reference momentum P_0, namely, $p_x = P_x/P_0$ and $p_y = P_y/P_0$, respectively. $z = -\beta c \Delta t$ where Δt is the time difference between the particle and the reference particle arriving at the azimuthal angle $\theta. \beta = v/c$, where v and c are the velocities of the particle and light, respectively. $\delta = \Delta P/P_0$ is the relative momentum deviation. The spin polarization of an electron bunch is the ensemble average of the $\hat{S}$.

In a circular accelerator running at a fixed energy, $\vec{\Omega}_0$ is a periodic function of θ, for which there is a unit-length periodic solution of Eq. (1), $\hat{n}_0(\theta)$, satisfying $\hat{n}_0(\theta + 2\pi) = \hat{n}_0(\theta)$. Then a spin vector $\hat{S}$ perpendicular to $\hat{n}_0$ precesses by a rotation angle $2\pi\nu_0$ in one revolution around $\hat{n}_0$, where ν_0 is called the closed-orbit spin tune. In a storage ring designed with a planar geometry and no solenoids (hereafter referred to as the "planar ring"), $\hat{n}_0(\theta)$ is close to the vertical direction, and $\nu_0 \approx a\gamma_0$, where $a = 0.00115965219$ for electrons (positrons), and γ_0 is the relativistic factor for the design energy.

These key concepts of the spin motion on the closed orbit can be extended to the more general phase-space coordinates. One special unit-length solution of Eq. (1) is the invariant spin field (ISF) [12], $\hat{n}(\vec{u};\theta)$, satisfying the periodicity condition $\hat{n}(\vec{u};\theta + 2\pi) = \hat{n}(\vec{u};\theta)$ and satisfying Eq. (1) along particle trajectories, $\vec{u}(\theta)$, obeying Hamilton's equations. Assuming that the orbital motion is integrable so that the orbital motion can be expressed in terms of action-angle variables, the analog of ν_0 for the combined betatron and synchrotron motion with orbital actions $\vec{I} \equiv (I_x, I_y, I_z)$, is the amplitude-dependent spin tune $\nu_s(\vec{I})$ describing the rate of spin precession around $\hat{n}$ [12]. The projection of the spin vector of a particle on the invariant spin field $J_S = \hat{S} \cdot \hat{n}$ is an adiabatic invariant of its spin motion [13]. On the closed orbit, $\hat{n}(\vec{u};\theta)$ and $\nu_s(\vec{J})$ reduce to $\hat{n}_0(\theta)$ and ν_0, respectively, but for typical orbital amplitudes with electrons $\nu_s(\vec{I}) \approx \nu_0$ in any case.

Machine imperfections and orbital oscillations contribute to $\Delta\vec{\Omega}(\theta)$ and $\vec{\omega}(\vec{u};\theta)$, respectively, and may perturb the spin motion in a resonant manner when the following condition of spin-orbit coupling resonances (spin resonances in short) is nearly satisfied:

$$\nu_s(\vec{I}) = k + k_x\nu_x + k_y\nu_y + k_z\nu_z, \qquad k, k_x, k_y, k_y \in Z, \tag{3}$$

where ν_x, ν_y, and ν_z are the horizontal and vertical betatron tunes, and the synchrotron tune, respectively. $\hat{n}(\vec{u};\theta)$ deviates from $\hat{n}_0(\theta)$ significantly near these spin resonances. As will be seen below, in perturbative estimates of spin motion, $\nu_s(\vec{I})$ is replaced by ν_0 in the above resonance condition. Note that the orbital tunes ν_x, ν_y, and ν_z, in the above definition of the spin resonances, are conventionally used in the case of weak couplings, reduced from the more general orbital tunes ν_I, ν_{II}, and ν_{III} obtained from the orbital eigenanalysis [14]. Spin resonances with $\nu_0 = k, k \in Z$ are called integer spin resonances. In a perfectly aligned planar ring with no solenoids $\hat{n}_0(\theta)$ is vertical. In a misaligned ring, $\hat{n}_0(\theta)$ can deviate strongly from the design direction when ν_0 is near an integer. Spin resonances with $|k_x| + |k_y| + |k_z| = 1$ and $|k_x| + |k_y| + |k_z| > 1$ are called first-order spin resonances and higher-order spin resonances, respectively.

Unlike polarized proton beams, which must be polarized at the source, e^+/e^- beams can also become spontaneously polarized in a storage ring by the emission of synchrotron radiation (the Sokolov-Ternov effect). In a perfectly aligned ring with no solenoids with vertical $\hat{n}_0$, the polarization is vertical, but in general, the polarization of the beam is along $\hat{n}_0$. The evolution of the beam polarization $P(t)$ in an electron storage ring for an initially unpolarized beam is

$$P(t) = P_\infty[1 - \exp(-t/\tau_p)], \tag{4}$$

where

$$P_\infty = \frac{-8}{5\sqrt{3}} \frac{\oint d\theta \frac{\hat{n}_0 \cdot \hat{b}}{|\rho|^3}}{\oint d\theta \frac{1 - \frac{2}{9}(\hat{n}_0 \cdot \hat{s})^2}{|\rho|^3}}, \tag{5}$$

where $\hat{s}$ is a unit vector along the particle's direction of motion, and $\hat{b} = \hat{s} \times \dot{\hat{s}}/|\dot{\hat{s}}|$, is the direction of the guiding magnetic field, which is normally vertical. P_∞ is the equilibrium beam polarization taking into account the orbital imperfections, but disregarding the radiative depolarization effect and the nonzero beam size [15]. The time constant of the Sokolov-Ternov effect, τ_p, is

$$\tau_p^{-1} \approx \frac{5\sqrt{3}}{8}\frac{r_e\gamma_0^5\hbar}{m_e}\frac{1}{2\pi}\oint d\theta\frac{1-\frac{2}{9}(\hat{n}_0\cdot\hat{s})^2}{|\rho|^3}. \tag{6}$$

In an ideal planar ring, P_∞ is 92.4%. In contrast, as mentioned, for an imperfect storage ring near integer values of ν_0, $\hat{n}_0$ may deviate from the vertical direction and lead to a reduced level of P_∞.

In addition to the Sokolov-Ternov effect, synchrotron radiation also causes radiative depolarization in electron storage rings, namely, the spin diffusion effect. It is implicit in standard literature [16,17] that the polarization at each point in phase space $\vec{u}$ is parallel to $\hat{n}(\vec{u};\theta)$. This is the so-called ISF approximation which we discuss again in Sec. VI. A photon emission perturbs the orbital motion and leads to a change in $\hat{n}$ and thus a slightly different $\hat{S}\cdot\hat{n}$. The stochastic nature of synchrotron radiation then leads to diffusion in $\hat{S}\cdot\hat{n}$ and thus a reduction of beam polarization [18], which has also been called "nonresonant spin diffusion" [19]. However, in the proximity of spin resonances, where $\hat{n}$ varies quickly with the particle's energy, $\hat{S}\cdot\hat{n}$ is no longer an invariant of motion, and it has been suggested that the above physics picture is no longer complete. Then a second mechanism, which could be important at very high energy, namely, the repetitive fast but "uncorrelated" crossing of the spin resonances, due to stochastic photon emissions, would be another source of radiative depolarization [20,21], which has also been called "resonant spin diffusion" [19]. In any case, the evolution of beam polarization in an electron storage ring is a compromise between the spontaneous polarization build-up and the radiative depolarization effects.

Analytical estimates of the equilibrium beam polarization in the presence of just nonresonant spin diffusion are generally made with the Derbenev-Kondratenko (DK) formula [16,17]:

$$P_{\mathrm{eq}} = \frac{-\frac{8}{5\sqrt{3}}\times\oint d\theta\langle\frac{1}{|\rho|^3}\hat{b}\cdot(\hat{n}-\frac{\partial\hat{n}}{\partial\delta})\rangle}{\oint d\theta\langle\frac{1}{|\rho|^3}[1-\frac{2}{9}(\hat{n}\cdot\hat{s})^2+\frac{11}{18}(\frac{\partial\hat{n}}{\partial\delta})^2]\rangle}, \tag{7}$$

where the $\langle\rangle$ brackets denote an average over the orbital phase space at azimuth θ. The spin-orbit coupling function $\partial\hat{n}/\partial\delta$ quantifies the depolarization. This can be rather large near spin resonances, leading to a reduced level of equilibrium polarization, as well as a smaller self-polarization build-up time τ_{tot} relative to τ_p

$$\tau_{\mathrm{tot}}^{-1} = \tau_p^{-1} + \tau_d^{-1}, \tag{8}$$

where τ_d is the time constant of the spin diffusion effect,

$$\tau_d^{-1} = \frac{5\sqrt{3}}{8}\frac{r_e\gamma_0^5\hbar}{m_e}\frac{1}{2\pi}\oint d\theta\left\langle\frac{\frac{11}{18}(\frac{\partial\hat{n}}{\partial\delta})^2}{|\rho|^3}\right\rangle. \tag{9}$$

The key to the evaluation of the DK formula lies in the evaluation of $\partial\hat{n}/\partial\delta$. As already indicated, in the derivation of the DK formula, only the first mechanism (nonresonant spin diffusion) of radiative depolarization was included. Then as suggested in [19,21], the DK formula should be augmented to take into account the effects of resonant spin diffusion too.

In a mainly planar storage ring, the equilibrium polarization can also be approximated by

$$P_{\mathrm{eq}} \approx \frac{P_\infty}{1+\frac{\tau_p}{\tau_d}}. \tag{10}$$

This equation disregards the tiny effect of kinetic polarization associated with the term $\hat{b}\cdot\frac{\partial\hat{n}}{\partial\delta}$ in Eq. (7) but captures the essentials of the trade-off between the Sokolov-Ternov effect and the radiative depolarization effect, regardless of the underlying mechanism of radiative depolarization. The strength of the depolarization effects is quantified by the ratio τ_p/τ_d.

So far, the evaluation of the equilibrium polarization in real storage rings has involved two classes of computer algorithms, as reviewed in detail in Refs. [22,23]. One class of algorithms numerically evaluates $\hat{n}$ and $\frac{\partial\hat{n}}{\partial\delta}$ and then applies Eq. (7) to calculate the equilibrium polarization. For example, SLIM [24] treats linearized orbital and spin motion and thus reflects the influence of first-order spin resonances while taking into account the effects of tilted $\hat{n}_0$ near integer values of ν_0. It can be classed as a first-order perturbative algorithm. Several other algorithms employ full three-dimensional spin motion [25–28] and thus expose the higher-order spin resonances resulting from that. Among these are the higher-order perturbative algorithm of Ref. [25] and the nonperturbative approaches of the SODOM algorithms [26,27].

The other class of algorithms evaluates the depolarization time τ_d through Monte Carlo simulations, like SITROS [29], SLICKTRACK [30], and BMAD [31,32], and then calculate the equilibrium polarization with Eqs. (5), (6), and (10). Unlike the previous class of algorithms, the Monte Carlo method, with its use of full three-dimensional spin motion, exposes both first-order and higher-order spin resonances automatically, while not relying on the calculation of $\hat{n}$ and $\frac{\partial\hat{n}}{\partial\delta}$ and Eq. (7). Nor is it dependent on other theories of spin diffusion. Therefore, the Monte Carlo method can be used to check theoretical models of radiative depolarization. The Monte Carlo method has the additional advantage that it can handle nonlinear orbital motion such as that caused by beam-beam forces.

Resonant and nonresonant spin diffusion for ultrahigh energy electron storage rings have been discussed in detail by Derbenev, Kondratenko, and Skrinsky [19]. These theories were later compared with the experiments with vertically polarized beams in the Large Electron-Positron (LEP) collider [33]. In the past decade, global interest has arisen in building future e^+e^- circular colliders. Mane worked out a scaling of equilibrium beam polarization at ultrahigh beam energies and studied possibilities for using Siberian snakes to mitigate the depolarization while retaining self-polarization at the same time [34]. Nikitin evaluated the radiative depolarization and the equilibrium transverse polarization in these super electron-positron circular colliders theoretically and discussed options for achieving longitudinally polarized colliding beams [35,36]. There are also attempts to reevaluate the radiative depolarization and equilibrium beam polarization using an approach based on the Bloch equation [37–39].

There have already been some simulations for the equilibrium polarization for the future circular e^+e^- colliders at ultrahigh energies. For example, Gianfelice-Wendt launched Monte Carlo simulations with the SITROS package [29] of the attainable self-polarization at CERN's Future Circular e^+e^- collider (FCC-ee) [40] at 45- and 80-GeV beam energies, aiming at energy calibration using RD. Quadrupole misalignments and beam-position-monitor errors were introduced in a simplified ring lattice without the interaction regions. It was shown that a reasonable polarization level can be achieved in the collider ring at both energies with a well-planned orbit correction scheme, while asymmetric wigglers are necessary to boost the self-polarization buildup at 45 GeV. Koop developed a Monte Carlo simulation code with a simplified model including one-turn energy-dependent spin precession and a lumped element to model spin perturbations, in addition to synchrotron oscillations and synchrotron radiation. This simulation code was also used to study the RD process [41].

On our side, a Monte Carlo simulation of radiative depolarization based on the Polymorphic Tracking Code (PTC) [42,43] was developed in Ref. [44]. The equilibrium beam polarization was simulated for a model ring lattice with a circumference of 50 km and artificial skew quadrupoles to excite betatron spin resonances. That study supported the suggestion in Ref. [19] that the spin dynamics enter an "uncorrelated regime" of spin resonance crossing at ultrahigh beam energies. However, it was not clear if this paradigm shift would exist in a realistic imperfect ring.

For this paper, we extend our studies to the radiative depolarization effects for the CEPC at the Z pole, as well as higher beam energies, and for various operation scenarios. We use a CEPC CDR lattice that contains two interaction regions and includes detailed error modeling and corrections. This lattice does not contain solenoids and has relatively weak orbital correctors with horizontal magnetic fields and belongs to the category of the "planar ring." We present the theories of radiative depolarization applicable to this case. Monte Carlo simulations based on the PTC code [42–44] were then applied to estimate the radiative depolarization effects, which are compared to those from the theories of radiative depolarization at ultrahigh beam energies.

This paper is arranged as follows: More details of theories of radiative depolarization in ultrahigh energy electron storage rings are reviewed in Sec. II. The setup of the CEPC lattice is introduced in Sec. III. In Sec. IV, the theories are applied to the CEPC lattice to evaluate the depolarization effects. Section V presents the results of Monte Carlo simulations for the equilibrium polarization for the standard CEPC lattice as well as for a lattice with asymmetric wigglers and a double rf system and these are compared with the results from theoretical models. The last section provides a summary of matters covered, conclusions, a commentary regarding the state of theory, and plans for future numerical work.

II. THEORIES OF RADIATIVE DEPOLARIZATION

In the following, we focus our analysis on realistic planar electron storage rings. Severe depolarization may occur when the closed-orbit spin tune ν_0 is near an integer k; so that $\hat{n}_0$ is tilted from the design direction, and then as shown below, the two first-order "parent" synchrotron spin resonances $\nu_0 \pm \nu_z = k$ can therefore be strong, even overlapping with each other. Depolarization also occurs near first-order parent betatron spin resonances $\nu_0 \pm \nu_r = k$, $r = x, y$. Moreover, even if ν_0 is not near an integer, its distance to adjacent integer spin resonances and first-order spin resonances is less than 220 MeV. As the spread of the spin precession frequency increases with the beam energy, it becomes more difficult to attain high polarization. In particular, as we show in the perturbation theory sketched below, higher-order synchrotron "sideband" spin resonances $\nu_0 \pm \nu_r + m\nu_z = k$, where m is an integer and $r = x, y, z$, become much more prominent, compared to those in lower-energy electron storage rings. The strongest of these resonances is centered on first-order parent spin resonances. Note that in this context, an integer spin resonance $\nu_0 = k$ will be a "sideband" spin resonance of the parent first-order synchrotron spin resonances $\nu_0 \pm \nu_z = k$. Note also that this kind of resonance can even occur when the ring is perfectly aligned and $\hat{n}_0$ is not tilted from the design direction, as, for example, when spin rotators make $\hat{n}_0$ horizontal in a region with quadrupoles and dispersion. The higher-order parent resonances also carry synchrotron sideband resonances.

Observations of beam polarization in electron storage rings have so far been in broad agreement with the expectations of Eq. (7), taking into account of the depolarization associated with these first-order and higher-order spin resonances. However, as already mentioned and as proposed in Refs. [19–21], the above picture with its consequences explored using perturbation theory belongs to the "nonresonant spin diffusion," while a somehow different picture of "resonant spin diffusion" is required for ultrahigh beam energies. This argument is better appreciated from a "dynamical" perspective as described in more detail below. Under certain circumstances, the combined influence of synchrotron oscillation and synchrotron radiation could lead to "repetitive fast but uncorrelated crossings" of the underlying spin resonances. Note that in this case, the influence of the resonant spin diffusion is not limited to the close proximity of the underlying spin resonances.

Now, to set the scene, we will first present the depolarization theory of the parent first-order spin resonances, or "first-order theory" in short. We explicitly derive the dominating contribution of first-order parent synchrotron spin resonances to radiative depolarization characterized by τ_p/τ_d and establish its connection with the strengths of tilts of $\hat{n}_0$ near integer values of ν_0. Then, we briefly review the theory of (high-order) synchrotron sideband spin resonances, referred to as the theory of the "correlated regime" in the following context. In these analyses, it will be shown that at ultrahigh beam energies, the synchrotron sideband spin resonances centered on integers are the most important contributors to depolarization. Following that, we will also refer to other, more detailed, perturbative calculations surrounding higher-order parent resonances and their sidebands. Then the theory of "uncorrelated regime" will also be reviewed. These theories will be compared to simulations in later sections.

To exhibit the depolarization effects of the first-order parent resonances and their sidebands in a storage ring with practical machine imperfections, we will now follow Yokoya's perturbative approach [45,46]. We denote the right-handed orthonormal set of unit-length solutions to Eq. (1) on the design orbit by $\hat{n}_{00}$, $\hat{m}_{00}$, and $\hat{l}_{00}$, where $|\Delta\vec{\Omega}| = |\vec{\omega}| = 0$, and define $\hat{k}_{00} = \hat{m}_{00} + i\hat{l}_{00}$. Then $\hat{k}_{00}(\theta) = e^{i(\Upsilon(\theta)-\Upsilon(\theta'))}\hat{k}_{00}(\theta')$, where $\Upsilon(\theta)$ is the spin precession phase. In a planar ring, $\Upsilon(\theta) \approx \nu_0\Phi(\theta)$, where $\Phi(\theta) = R\int_0^\theta \frac{1}{\rho_x}d\theta$ is the integral of the bending angle between the azimuthal angles 0 and θ, R is the average radius of the storage ring, ρ_x is the radius of curvature for the local orbit. In a perfect planar ring, $\hat{n}_{00}$ is in the vertical direction while $\hat{k}_{00}$ is in the horizontal plane, respectively. Considering the perturbed fields on the closed orbit, $|\Delta\vec{\Omega}| \neq 0$, $|\vec{\omega}| = 0$, we denote the right-handed orthonormal set of unit-length solutions of Eq. (1) as $[\hat{n}_0(\theta), \hat{m}_0(\theta), \hat{l}_0(\theta)]$, and define $\hat{k}_0(\theta) = \hat{m}_0(\theta) + i\hat{l}_0(\theta)$. Then $\hat{n}_0$ and $\hat{k}_0$ can be expanded as $\hat{n}_0 = \hat{n}_{00} + \Delta\hat{n}_{00}$ and $\hat{k}_0 = \hat{k}_{00} + \Delta\hat{k}_{00}$. The vector $\hat{k}_0$ is quasiperiodic,

$$\hat{k}_0(\theta + 2\pi) = e^{i2\pi\nu_0}\hat{k}_0(\theta). \tag{11}$$

When $|\Delta\vec{\Omega}| \neq 0$, $|\vec{\omega}| \neq 0$, $\hat{n}$ can be expressed by

$$\hat{n}(\vec{u};\theta) = \hat{n}_0\sqrt{1 - |\zeta(\vec{u};\theta)|^2} + \mathcal{R}[\hat{k}_0^\star\zeta(\vec{u};\theta)], \tag{12}$$

where $\hat{k}_0^\star$ is the complex conjugate of $\hat{k}_0$, and $\zeta(\vec{u}(\theta);\theta)$ satisfies

$$\frac{d\zeta}{d\theta} = -i\vec{\omega}\cdot\hat{k}_0\sqrt{1-|\zeta|^2} + i\vec{\omega}\cdot\hat{n}_0\zeta. \tag{13}$$

To arrive at our chosen set of resonances, we choose $|\zeta| \ll 1$. Then the solution for $\zeta(\vec{u};\theta)$ to Eq. (13) at $(\vec{u};\theta)$ with $\zeta(\vec{u};\theta) = \zeta(\vec{u};\theta + 2\pi)$ is

$$\zeta(\vec{u};\theta) = -ie^{-i\chi(\vec{u};\theta)}\underset{\epsilon\to+0}{\mathrm{Lim}}\left[\int_{-\infty}^{\theta} e^{\epsilon\theta'}\, e^{i\chi(\vec{u}(\theta');\theta')} \times \vec{\omega}(\vec{u}(\theta');\theta')\cdot\hat{k}_0(\theta')d\theta'\right], \tag{14}$$

where

$$\chi(\vec{u};\theta) = \underset{\epsilon\to+0}{\mathrm{Lim}}\left[-\int_{-\infty}^{\theta} e^{\epsilon\theta'}\vec{\omega}(\vec{u}(\theta');\theta')\cdot\hat{n}_0(\theta')d\theta'\right]. \tag{15}$$

The integral from $-\infty$ in these expressions can be appreciated as follows as an instance of the "antidamping" procedure using the adiabatic invariance of $J_S = \hat{S}\cdot\hat{n}$ [25,47–49]. A particle is placed infinitesimally close to the closed orbit in the infinite "past" with $\hat{S}\cdot\hat{n}_0 = 1$. The particle and its spin are then tracked forward up to θ while the orbital amplitudes and the perturbation to the spin increase very slowly and exponentially. Then at θ, $\hat{n}$ is given by the final $\hat{S}$ [25].

As will be shown below, the first-order parent spin resonances are driven by the perturbation term $\vec{\omega}\cdot\hat{k}_0$, while the higher-order synchrotron "sideband" spin resonances are due to the modulation of the rate of spin precession around $\hat{n}_0$ driven by $\vec{\omega}\cdot\hat{n}_0$. The spin-orbit coupling function can be obtained as

$$\frac{\partial\hat{n}}{\partial\delta} \approx \mathcal{R}\left(\hat{k}_0^\star\frac{\partial\zeta}{\partial\delta}\right). \tag{16}$$

A. First-order parent spin resonances

Considering the spin resonances up to the first order, the solution for ζ is

$$\zeta(\vec{u};\theta) \approx \underset{\epsilon\to+0}{\mathrm{Lim}}\left[-i\int_{-\infty}^{\theta} e^{\epsilon\theta'}\vec{\omega}\cdot\hat{k}_0 d\theta'\right], \tag{17}$$

where for this, $\vec{\omega}$ is linearized with respect to the betatron coordinates r_β, $r = x$, y, as well as the synchrotron coordinate δ, and decomposed into three oscillation modes [46]:

$$\vec{\omega} = \vec{\omega}_z\delta + \vec{\omega}_x x_\beta + \vec{\omega}_y y_\beta \tag{18}$$

with

$$\begin{aligned}\vec{\omega}_z &= -R\left[(1+a\gamma_0)(G_x\eta_x + Q_y\eta_y) - \frac{1}{\rho_x}\right]\vec{e}_y \\ &\quad + R\left[(1+a\gamma_0)(G_y\eta_y + Q_x\eta_x) - \frac{1}{\rho_y}\right]\vec{e}_x \\ \vec{\omega}_x &= -R(1+a\gamma_0)(G_x + Q_y)\vec{e}_y \\ \vec{\omega}_y &= R(1+a\gamma_0)(G_y + Q_x)\vec{e}_x. \end{aligned} \tag{19}$$

The ρ_y is the vertical radius of curvature for the local orbit, which could be due to vertical quadrupole misalignment errors, dipole roll errors, or orbital correctors. Finally, η_x, η_y are the dispersion functions and the focusing gradients of quadrupoles or dipoles are expressed as $G_x = \frac{e}{P_0}\frac{\partial B_y}{\partial x} + \frac{1}{\rho_x^2}$, $G_y = \frac{e}{P_0}\frac{\partial B_x}{\partial y} + \frac{1}{\rho_y^2}$, while the gradients of skew quadrupoles and inclined dipoles are expressed as $Q_x = \frac{e}{P_0}\frac{\partial B_x}{\partial x} - \frac{1}{\rho_x\rho_y}$, $Q_y = \frac{e}{P_0}\frac{\partial B_y}{\partial y} + \frac{1}{\rho_x\rho_y}$.

Then Eq. (17) can be analyzed separately for each oscillation mode with the integral of each mode amounting to a resonant term times a one-turn integral. The contributions of betatron oscillation modes $\vec{\omega}_r \cdot r_\beta$, $r = x, y$ to ζ are

$$\begin{aligned}\zeta_r(I_r, \psi_r; \theta) &= \operatorname*{Lim}_{\epsilon\to+0}\left[-i\int_{-\infty}^{\theta} e^{\epsilon\theta'}\vec{\omega}_r r_\beta \cdot \hat{k}_0 d\theta'\right] \\ &= \sum_{\pm}\frac{i\sqrt{I_r/2}}{e^{-2\pi i(\nu_0 \pm \nu_r)} - 1}F_{\pm r}(\psi_r; \theta)\end{aligned} \tag{20}$$

with

$$F_{\pm r}(\psi_r; \theta) = \int_{\theta-2\pi}^{\theta}\vec{\omega}_r \cdot \hat{k}_0\sqrt{\beta_r}e^{\pm i(\psi_r + \tilde{\Psi}_r)}d\theta' \tag{21}$$

after using the quasiperiodicity of $\hat{k}_0(\theta)$, and where the angle ψ_r is evaluated at θ while r_β is expressed in terms of action-angle variables I_r and ψ_r as

$$r_\beta = \sqrt{2I_r\beta_r}\cos(\psi_r + \tilde{\Psi}_r) \tag{22}$$

and where β_r is the betatron function and $\tilde{\Psi}_r$ is

$$\tilde{\Psi}_r = R\int_0^{\theta}\frac{d\theta'}{\beta_r} - \nu_r\theta \tag{23}$$

at the azimuth θ. Similarly, and in a usually good approximation that synchrotron motion is simply harmonic with a θ-independent β_z, the contribution from the synchrotron mode to ζ is

$$\begin{aligned}\zeta_z(I_z, \psi_z; \theta) &= \operatorname*{Lim}_{\epsilon\to+0}\left[-i\int_{-\infty}^{\theta} e^{\epsilon\theta'}\vec{\omega}_z\delta \cdot \hat{k}_0 d\theta'\right] \\ &= \sum_{\pm}\frac{i\sqrt{I_z/2}}{e^{-2\pi i(\nu_0 \pm \nu_z)} - 1}F_{\pm\delta}(\psi_z; \theta)\end{aligned} \tag{24}$$

with

$$F_{\pm\delta}(\psi_z; \theta) = \int_{\theta-2\pi}^{\theta}\vec{\omega}_z \cdot \hat{k}_0\sqrt{\beta_z}e^{\pm i\psi_z}d\theta', \tag{25}$$

where I_z and ψ_z are the action-angle variables of the synchrotron oscillation, $\psi_z = \psi_{z0} + \nu_z\theta$ and

$$\delta = \sqrt{2I_z\beta_z}\cos(\psi_z). \tag{26}$$

Equations (20) and (24) reveal first-order parent betatron spin resonances and first-order parent synchrotron spin resonances, respectively. The one-turn integrals $F_{\pm r}$ and $F_{\pm\delta}$ reflect the strengths of these spin resonances. Comparison of the above formulas for first-order resonances with those under the topic "Reformulation in terms of beta functions and dispersion" in Ref. [22] shows that we are, in effect, using the "betatron-dispersion" version of the SLIM formalism.

In ultrahigh energy electron storage rings, the betatron oscillations complete many periods in one revolution, namely, $\nu_x, \nu_y \gg 1$. Hence the one-turn integrals $F_{\pm r}$ tend to be small. In contrast, $\nu_z \ll 1$. Then the synchrotron phase changes relatively little over one turn so that the integrals $F_{\pm\delta}$ need not be so small. Therefore, first-order parent betatron spin resonances can be much weaker than the first-order parent synchrotron spin resonances.

So we next focus on the pair of first-order parent synchrotron spin resonances centered on an integer value, k, of ν_0. The spin-orbit coupling function can be approximated by

$$\frac{\partial\hat{n}}{\partial\delta} \approx \frac{1}{2}\mathcal{R}[\hat{k}_0^\star \cdot (D_{+z} + D_{-z})] \tag{27}$$

with

$$D_{\pm z}(\theta) = \frac{ie^{\mp i\nu_z\theta}}{e^{-2\pi i(\nu_0 \pm \nu_z)} - 1}\int_{\theta-2\pi}^{\theta}\vec{\omega}_z \cdot \hat{k}_0 e^{\pm i\nu_z\theta'}d\theta'. \tag{28}$$

There are two different driving terms in the presence of machine imperfections. The first is from the projection of the vertical component of $\vec{\omega}_z$ onto $\hat{k}_0$. Near an integer value of ν_0, $\hat{k}_0$ deviates from the horizontal plane, and $\vec{e}_y \cdot \hat{k}_0$ is actually related to the strength, $\tilde{\omega}_k$, of the integer resonance in the tilt of $\hat{n}_0$. In fact, as shown in detail in the Appendix (Sec. A 1),

$$
\begin{aligned}
\vec{e}_y \cdot \hat{k}_0 &= i \sum_{k=-\infty}^{\infty} \frac{\tilde{\omega}_k e^{i(\nu_0 - k)\theta'}}{\nu_0 - k} \\
\tilde{\omega}_k &= \frac{1}{2\pi} \int_0^{2\pi} \Delta\Omega_x e^{i\nu_0(\Phi(\theta') - \theta') + ik\theta'} d\theta' \\
\Delta\Omega_x &= -R(1 + a\gamma_0)\left(y_{\mathrm{COD}} \cdot G_y + x_{\mathrm{COD}} \cdot Q_x + \frac{1}{\rho_y}\right),
\end{aligned}
\tag{29}
$$

where x_{COD} and y_{COD} are the horizontal and vertical closed-orbit distortions, respectively, and the feed-down effect of normal quadrupoles generally dominates $\Delta\Omega_x$, and where the denominator $\nu_0 - k$ accounts for the resonant behavior. In proton and electron rings, in the context of acceleration, the $\tilde{\omega}_k$ are also the strengths of the so-called "imperfection resonances." With the neglect of the terms $1/\rho_x$ and $Q_y\eta_y$, the vertical component of $\vec{\omega}_z$ can be expanded into a Fourier series

$$
-(1 + a\gamma_0) R G_x \eta_x = \sum_{j=-\infty}^{\infty} \xi_j e^{-ij\theta}. \tag{30}
$$

Then by inserting Eqs. (30), (29), and (28) into Eq. (27), we obtain

$$
\frac{\partial \hat{n}}{\partial \delta}(\theta) \approx \mathcal{R}\left[\hat{k}_0^{\star} \cdot \sum_{\substack{k=-\infty \\ j=-\infty}}^{+\infty} \frac{-i\tilde{\omega}_k \xi_j (\nu_0 - k - j) e^{i(\nu_0 - k - j)\theta}}{(\nu_0 - k)[(\nu_0 - k - j)^2 - \nu_z^2]}\right] \tag{31}
$$

and

$$
\left|\frac{\partial \hat{n}}{\partial \delta}(\theta)\right|^2 \approx \left|\sum_{\substack{k=-\infty \\ j=-\infty}}^{+\infty} \frac{\tilde{\omega}_k \xi_j (\nu_0 - k - j) e^{i(\nu_0 - k - j)\theta}}{(\nu_0 - k)((\nu_0 - k - j)^2 - \nu_z^2)}\right|^2. \tag{32}
$$

Note that

$$
\frac{\tau_p}{\tau_d} \approx \frac{11}{18} \oint d\theta \frac{(\frac{\partial \hat{n}}{\partial \delta})^2}{|\rho|^3} \Big/ \oint d\theta \frac{1}{|\rho|^3}. \tag{33}
$$

When averaged around the ring, the cross terms vanish in Eq. (32) so that the depolarization effect is described as

$$
\frac{\tau_p}{\tau_d} \approx \frac{11}{18} \sum_{\substack{k=-\infty \\ j=-\infty}}^{+\infty} \frac{|\tilde{\omega}_{k-j}|^2 |\xi_j|^2 (\nu_0 - k)^2}{(\nu_0 - k + j)^2 [(\nu_0 - k)^2 - \nu_z^2]^2}. \tag{34}
$$

Generally, the evaluation of Eq. (34) requires retaining a sufficient number of k and j terms, after a check of convergence. However, in ultrahigh energy electron storage rings with typical layouts such as that of the CEPC, and as shown in the Appendix (Sec. A 2), where we study the structure of ξ_j in a simplified model lattice following the approach in Ref. [50], in Eq. (34), the Fourier harmonic $\xi_0 \approx -(1 + a\gamma_0)$, is the major contributor to the Fourier expansion for the contribution of horizontal dispersion to depolarization. Let us denote the integer part of ν_0 by n so that only a few Fourier harmonics of $\tilde{\omega}_k$ with $|k - n| \le l$ have a strong influence, where l is a small positive integer to be determined as a result of a check of convergence. Then the depolarization effect can be approximated by

$$
\frac{\tau_p}{\tau_d} \approx \frac{11}{18} \sum_{k=n-l}^{n+l} \frac{\nu_0^2 |\tilde{\omega}_k|^2}{[(\nu_0 - k)^2 - \nu_z^2]^2}. \tag{35}
$$

Normally, $\nu_z \ll 1$ in high-energy electron storage rings. Then when ν_0 is chosen to be far from the first-order parent synchrotron spin resonances, Eq. (35) can be approximated by

$$
\frac{\tau_p}{\tau_d} \approx \frac{11}{18} \sum_{k=n-l}^{n+l} \frac{\nu_0^2 |\tilde{\omega}_k|^2}{(\nu_0 - k)^4}. \tag{36}
$$

Equation (36) agrees with the result [51] in Refs. [19,52]. Equation (36) does not apply when ν_0 is near first-order parent synchrotron spin resonances while Eq. (35) is still applicable.

The second driving term arises from nonzero vertical dispersion, mainly due to vertical closed-orbit distortions in quadrupoles, and also due to roll errors of dipoles, as well as vertical orbital correctors, which all contribute to the projection of the horizontal component of $\vec{\omega}_z$ onto $\hat{k}_0$ [53]. With the neglect of the terms $1/\rho_y$ and $Q_x\eta_x$, the projection of the horizontal component of $\vec{\omega}_z$ on $\hat{k}_0$ can be expanded into a Fourier series

$$
(1 + a\gamma_0) R G_y \eta_y \vec{e}_x \cdot \hat{k}_0 = \sum_{k=-\infty}^{\infty} \tilde{\lambda}_k e^{i(\nu_0 - k)\theta}, \tag{37}
$$

where

$$
\tilde{\lambda}_k = \frac{1}{2\pi} \int_0^{2\pi} (1 + a\gamma_0) R G_y \eta_y e^{i\nu_0(\Phi(\theta') - \theta') + ik\theta'} d\theta'. \tag{38}
$$

Then the depolarization effect is described by [53]

$$
\frac{\tau_p}{\tau_d} \approx \frac{11}{18} \sum_{k=n-l}^{n+l} \frac{(\nu_0 - k)^2 |\tilde{\lambda}_k|^2}{[(\nu_0 - k)^2 - \nu_z^2]^2}. \tag{39}
$$

Now in this regime of weak coupling, we combine these two different contributions to τ_p/τ_d to evaluate the depolarization effect due to the parent first-order synchrotron resonances as

$$\frac{\tau_p}{\tau_d} \approx \frac{11}{18} \sum_{k=n-l}^{n+l} \frac{\nu_0^2 |\tilde{\omega}_k|^2 + (\nu_0 - k)^2 |\tilde{\lambda}_k|^2}{[(\nu_0 - k)^2 - \nu_z^2]^2}. \tag{40}$$

In practice, only a few harmonics in the above formulas dominate and they could be partially compensated, and then the tilt of $\hat{n}_0$ reduced, with specially arranged correction coils forming closed-orbit vertical bumps [54] chosen to generate "anti-harmonics." These so-called harmonic closed-orbit spin matching techniques [55,56] have been shown to be essential for improving the equilibrium beam polarization level.

In this paper, we focus on comparing the polarization theory and simulations, applied to the imperfect CEPC lattices without taking account of the harmonic closed-orbit spin matching. Considering only the first-order parent spin resonances, the equilibrium beam polarization can be analytically evaluated using Eqs. (5), (10), and (40).

B. Higher-order synchrotron sideband spin resonances

As shown previously, the first-order parent spin resonances arise from the perturbation term $\vec{\omega} \cdot \hat{k}_0$. In addition, the spin precession rate is dependent on the coordinates of orbital motion, and orbital oscillations induce modulations of the spin precession rate, which lead to the higher-order "sideband" resonances of these first-order parent spin resonances. This can be seen from Eq. (14), where $\chi(\theta)$, as an integral of $\vec{\omega} \cdot \hat{n}_0$, can also be expressed as a resonant term times a one-turn integral, representing the average modulation over one turn [45,46]. Then betatron tunes are so large that their one-turn integrals are small and the corresponding sideband spin resonances are insignificant. In contrast, the synchrotron tune is tiny and the average modulation cannot be ignored.

In particular, around each integer k, there can be an infinite number of higher-order synchrotron sideband spin resonances in the form of $\nu_0 \pm m\nu_z = k$. The overall depolarization effects of this family of spin resonances can be incorporated by multiplying the τ_p/τ_d contribution of the first-order parent synchrotron spin resonances around integer k by a depolarization enhancement factor $\mathcal{F}_k$ [45]

$$\mathcal{F}_k = ((\nu_0 - k)^2 - \nu_z^2)^2 \sum_m \frac{e^{-\sigma^2} I_m(\sigma^2)}{[(\nu_0 - k - m\nu_z)^2 - \nu_z^2]^2}, \tag{41}$$

where I_m is the modified Bessel function with the modulation index σ defined as

$$\sigma = \frac{\sigma_0}{\nu_z} = \frac{\nu_0 \sigma_\delta}{\nu_z} \tag{42}$$

and where $\sigma_0 = \nu_0 \sigma_\delta$ measures the spread of the instantaneous spin precession frequencies in a planar ring for the rms relative energy spread, σ_δ, resulting from synchrotron radiation. Note that in the derivation of Eq. (41), it was also assumed that synchrotron motion is approximately harmonic so that Eq. (26) holds.

The modulation index σ reflects the spread of spin precession frequencies in a beam, relative to the spacing of adjacent synchrotron sideband spin resonances. For a fixed ν_z, σ scales with ${\gamma_0}^2$, and higher-order synchrotron sideband spin resonances become more prominent at higher beam energies. To achieve a higher equilibrium beam polarization level, it is essential to mitigate the influence of these important synchrotron sideband spin resonances. It is customary to choose $[a\gamma_0] \approx 0.5$ where here and later $[x]$ denotes the fractional part of $x \in R$.

Considering both the first-order and higher-order synchrotron spin resonances, the depolarization effect can be evaluated as

$$\frac{\tau_p}{\tau_d} \approx \frac{11}{18} \sum_{k=n-l}^{n+l} \sum_{m=-\infty}^{\infty} \left(\frac{\nu_0^2 |\tilde{\omega}_k|^2 e^{-\sigma^2} I_m(\sigma^2)}{[(\nu_0 - k - m\nu_z)^2 - \nu_z^2]^2} + \frac{(\nu_0 - k)^2 |\tilde{\lambda}_k|^2 e^{-\sigma^2} I_m(\sigma^2)}{[(\nu_0 - k - m\nu_z)^2 - \nu_z^2]^2} \right). \tag{43}$$

For further treatments of higher-order resonances using perturbation theory, see Refs. [25,57–59].

C. The correlated and uncorrelated regimes of resonance crossing

Reference [19] distinguishes between two regimes, namely, the so-called nonresonant and resonant spin diffusion. In a modern treatment, we would focus on the invariant spin field $\hat{n}(\vec{u};\theta)$ and the amplitude-dependent spin tune $\nu_s(\vec{J})$ for the combined betatron and synchrotron motion. The amplitude-dependent spin tune is constant during such motion for fixed orbital amplitudes but changes if, for example, the amplitude of the synchrotron motion changes due to photon emission. However, in Ref. [19], a hybrid approach is adopted whereby the invariant spin field $\hat{n}$ is explicitly time-independent and the synchrotron motion is added by hand so that the instantaneous spin-precession rate ν is dependent on the instantaneous energy deviation of a particle, i.e., $\nu \approx \nu_0(1+\delta)$. Since $\nu_z \ll 1$ in most electron storage rings, ν looks like a slowly varying ν_0. In this "dynamical" picture, some underlying spin resonances could be crossed as a result of synchrotron oscillations, or synchrotron radiation, or the combined effect. As far as we know Ref. [19] is the most recent work on these topics. So to facilitate comparison, we adopt that approach and argumentation too.

As already mentioned in Sec. II B, stochastic photon emissions cause a random walk in particle energies and thus lead to a spread in particle energies and a spread in spin precession frequencies characterized by $\sigma_0 = \nu_0 \sigma_\delta$. The parameter σ_0 also characterizes the amplitude of variation of the spin precession rate of an arbitrary particle in the beam, as a result of synchrotron radiation and synchrotron oscillation. At low energy, typically $\sigma_0 \ll 1$, in particular, when $\sigma_0 \ll \nu_z$, the design energy can be set so that the $\nu_s(\vec{J})$ of beam particles sit between important spin-orbit resonances. Then the perturbation theory of Sec. II B above can be used to get the first estimates of τ_p/τ_d and the sidebands will be narrow according to Sec. II B. This is the regime called nonresonant spin diffusion in Ref. [19].

At higher beam energies, σ_0 becomes larger so that some beam particles inevitably cross some important spin-orbit resonances in the process of synchrotron radiation and synchrotron oscillation. Then there can be so-called resonant spin diffusion. In particular, it was argued in Ref. [19] that when the diffusion of the spin-precession phase advance introduced by stochastic photon emissions is negligible in one synchrotron period, the crossings of an underlying spin resonance during precession-rate oscillations, driven by synchrotron oscillations, are correlated. Then, according to Ref. [19], the perturbation theory of Sec. II B can still be used. This poses a constraint on the "correlation index" κ, which characterizes the spread in the spin-precession phase advance in a synchrotron period,

$$\kappa = \frac{\nu_0^2 \lambda_p}{\nu_z^3} \ll 1, \tag{44}$$

where λ_p is the normalized polarizing rate,

$$\lambda_p = \tau_p^{-1} \frac{R}{c}. \tag{45}$$

Note that following Ref. [19], we have

$$\sigma^2 = \frac{\sigma_0^2}{\nu_z^2} = \frac{\nu_0^2 \sigma_\delta^2}{\nu_z^2} = \frac{11}{36} \frac{\nu_0^2 \lambda_p}{\nu_z^2 \Lambda_z},$$

where Λ_z is the damping decrement for longitudinal motion,

$$\Lambda_z = \tau_z^{-1} \frac{R}{c}, \tag{46}$$

where τ_z is the longitudinal damping time. Then since $\Lambda_z \ll \nu_z$, the above constraint on κ is more relaxed than the earlier constraint on σ_0/ν_z.

The perturbative depolarization theory of higher-order synchrotron sideband spin resonances will be hereafter referred to as the theory of the "correlated regime" of spin resonance crossing (or in short the "correlated regime").

In contrast, if the radiation is extremely violent, or the synchrotron tune is very small, the condition in Eq. (44) could be violated. Then if $\sigma_0 \gg \nu_z$ also holds, successive crossings of the underlying spin resonance in synchrotron oscillations become completely uncorrelated. In this case, it was suggested in Ref. [19] that the normalized depolarization rate λ_d due to the photon emissions can be evaluated by [20]

$$\lambda_d = \pi \sum_k \langle |\tilde{\epsilon}_k|^2 \delta(\nu - k) \rangle, \tag{47}$$

where $\delta(\nu - k)$ is the delta function, ν is the instantaneous spin-precession rate, $\tilde{\epsilon}_k$ denotes the strength of spin resonances on general synchrobetatron trajectories, and $\langle\rangle$ is the average over the beam particles. In ultrahigh energy planar electron storage rings, the $\tilde{\omega}_k$, of the integer resonances in the tilt of $\hat{n}_0$, was regarded [19] as the major contribution to $\tilde{\epsilon}_k$. Then assuming $\nu \approx \nu_0(1+\delta)$ and considering a Gaussian distribution for δ, the depolarization effect can be evaluated as [19]

$$\frac{\tau_p}{\tau_d} \approx \frac{\sqrt{\pi/2}}{\lambda_p} \sum_{k=n-l}^{n+l} \frac{|\tilde{\omega}_k|^2}{\sigma_0} \exp\left[-\frac{(\nu_0 - k)^2}{2\sigma_0^2}\right]. \tag{48}$$

This spin diffusion theory will be hereafter referred to as the "uncorrelated regime."

It was also suggested in Ref. [19] that, when $\sigma_0 \ll 1$, the spin diffusion due to the uncorrelated resonance crossing is comparable to that due to the "trembling" of the $\hat{n}$ associated with photon emissions and that the total depolarization effect can then be evaluated by adding Eqs. (48) to (36). Note that Eq. (36) does not include the depolarization effect from the synchrotron sideband spin resonances. In addition, when $\sigma_0 \gg 1$, it was also predicted in Ref. [19] that there would be no resonant dependence of spin diffusion on energy, and beam polarization would grow with energy.

The theories of the "correlated regime" and "uncorrelated regime" lead to quite distinct depolarization effects, while the condition of their application is quite vaguely defined. In particular, there is no definite boundary of κ at which the depolarization effect enters the uncorrelated regime. Moreover, it is not clear either what theory of radiative depolarization is applicable between the correlated regime and the uncorrelated regime. Note that the theory of the correlated regime has been verified in LEP experiments [56], but the theory of the uncorrelated regime seems to be beyond the parameter space of LEP [56].

III. CEPC LATTICE SETUP

We now continue by describing simulations of the equilibrium beam polarization for the CEPC CDR lattice [3]. For these, the major contributions of misalignment errors and relative field errors of magnets, listed in Table I, were introduced into the lattice. These errors follow a Gaussian distribution truncated at ±3σ. Then, a detailed closed orbit and optics correction scheme was developed [60] to recover the lattice performance, using the SAD [61] and Accelerator Toolbox (AT) [62] codes. BPM errors were not yet included in the correction scheme.

About 1500 correctors in both the horizontal and vertical planes were used for the closed-orbit distortion (COD)

TABLE I. CEPC magnets' error settings in the simulations.

	Misalignment error			
Component	Δx(μm)	Δy(μm)	$\Delta\theta_z$(μrad)	Field error
Dipole	0	0	0	0.01%
Arc quadrupole	100	100	100	0.02%
IR quadrupole	50	50	50	0
Sextupole	100	100	100	0

correction. The horizontal correctors and vertical correctors were placed next to focusing quadrupoles and defocusing quadrupoles, respectively. About 1500 beam position monitors were placed next to quadrupoles, four per betatron wave period. Both the root-mean-squared (rms) values of the horizontal and vertical closed orbits are smaller than 50 μm after the COD correction. Skew quadrupole coils on sextupoles and some independent skew quadrupoles were used to minimize the vertical dispersion and the betatron coupling. Since the detector solenoids in the interaction regions are not yet included in the lattice, the vertical emittance after correction is 2.5×10^{-3} pm · rad at the Z pole after the coupling correction. It is much smaller than the target value, 1.6 pm · rad, in the CDR.

To properly account for the parent betatron spin resonances in the equilibrium polarization simulations, the vertical emittance of the imperfect lattice was adjusted to the target value as follows. According to a separate analysis [3], the coupling contribution due to the detector solenoid fringe field is around 28% of the target vertical emittance assuming that the detector solenoid field is 2 T during Z operation. Zero-length skew quadrupoles SQ1 and SQ2 were added next to the final focusing doublet Q1 and Q2, respectively, to account for the solenoid fringe field contribution, as illustrated in Fig. 1(b). The integral field gradients of SQ1 and SQ2 are 6.4×10^{-5} and 3.7×10^{-6} m^{-1} respectively. To generate the remaining 72% targeted vertical emittance, all quadrupoles in the four straight section regions, as shown in Fig. 1(a), were rotated by the same angle, 0.2° in the lattice.

Figure 2 shows the closed orbit and the beta beating along the CEPC lattice in the horizontal and vertical directions obtained by SAD. The rms values of the horizontal closed orbit and vertical closed orbit are 37 and 28 μm, respectively. The rms values of the horizontal and vertical beta beatings are 0.36% and 3.4%, respectively. We are aware that BPM errors, in particular, the relative offset errors between BPMs and adjacent quadrupole magnets, once introduced, would worsen the attainable level of closed-orbit distortions after correction and also affect the performance after optics correction. These effects would in turn affect the equilibrium beam polarization level. These BPM errors and other error sources will be included properly in future studies and set the basis for a more practical prediction of the attainable equilibrium beam polarization level. In this study, the focus is to reveal the mechanisms of radiative depolarization, rather than to predict the attainable equilibrium beam polarization level.

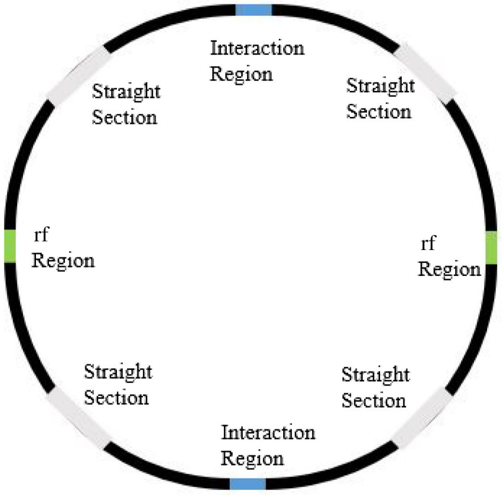

(a) Straight sections of the CEPC

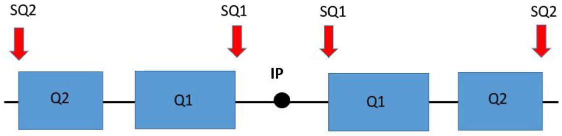

(b) Locations of SQ1 and SQ2 in one interaction region

FIG. 1. The layout of the CEPC straight sections and locations of coupling adjustment components. In (a), the eight straight sections of the CEPC include two interaction regions (blue), two rf regions (blue), and four straight sections (gray) for other purposes. The quadrupoles in these four straight sections are artificially rotated to generate the transverse coupling. In (b), zero-length skew quadrupoles SQ1 and SQ2 are inserted next to the final focus quadrupoles Q1 and Q2 around each of the two interaction points, to account for the transverse coupling introduced by the detector solenoids.

Most of the CEPC accelerator design and simulations were based on SAD [61]. However, the capability to simulate beam polarization is still under development in SAD. Then, in this paper, the Bmad and PTC codes were used in the simulation of equilibrium beam polarization. PTC is embedded inside Bmad as a library, and much effort has been invested, by the authors of both codes, to make the interface almost seamless. Bmad has a built-in module to simulate the equilibrium beam polarization with contributions from just the first-order spin resonances. This module calls PTC internally to construct the linearized orbital and spin transport matrices and then evaluate $\hat{n}_0$ and $\frac{\partial \hat{n}}{\partial \delta}$, using the SLIM formalism [24]. To go further, Monte Carlo simulations of the depolarization effects were studied using PTC [44] so that the influence of high-order spin resonances was exposed. Both approaches were adopted in the study of the equilibrium beam polarization of the CEPC.

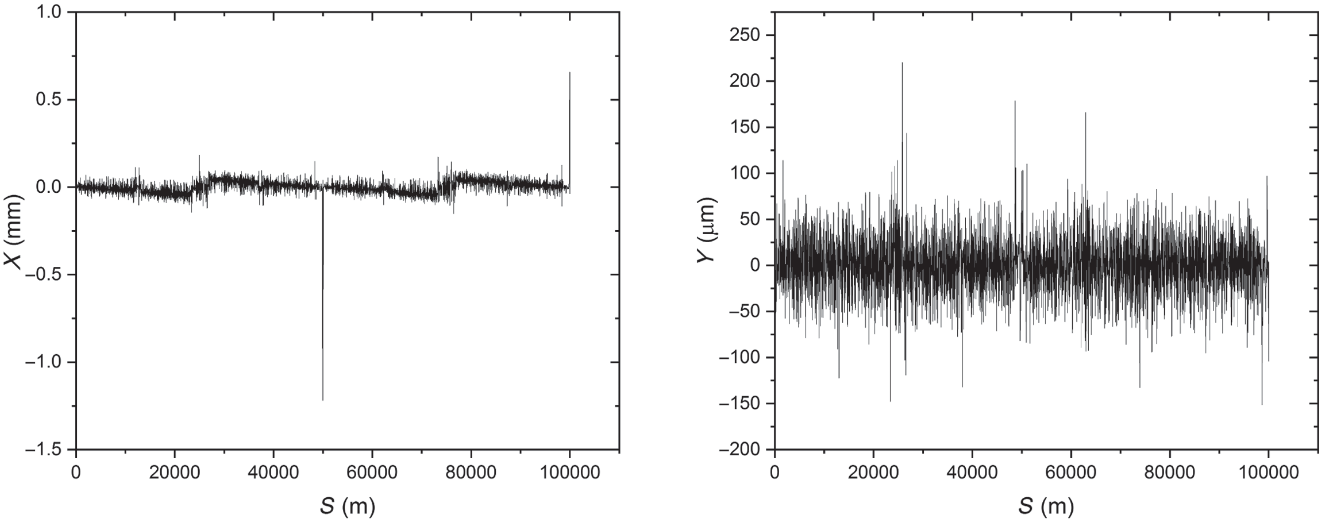

(a) Horizontal closed orbit.

(b) Vertical closed orbit.

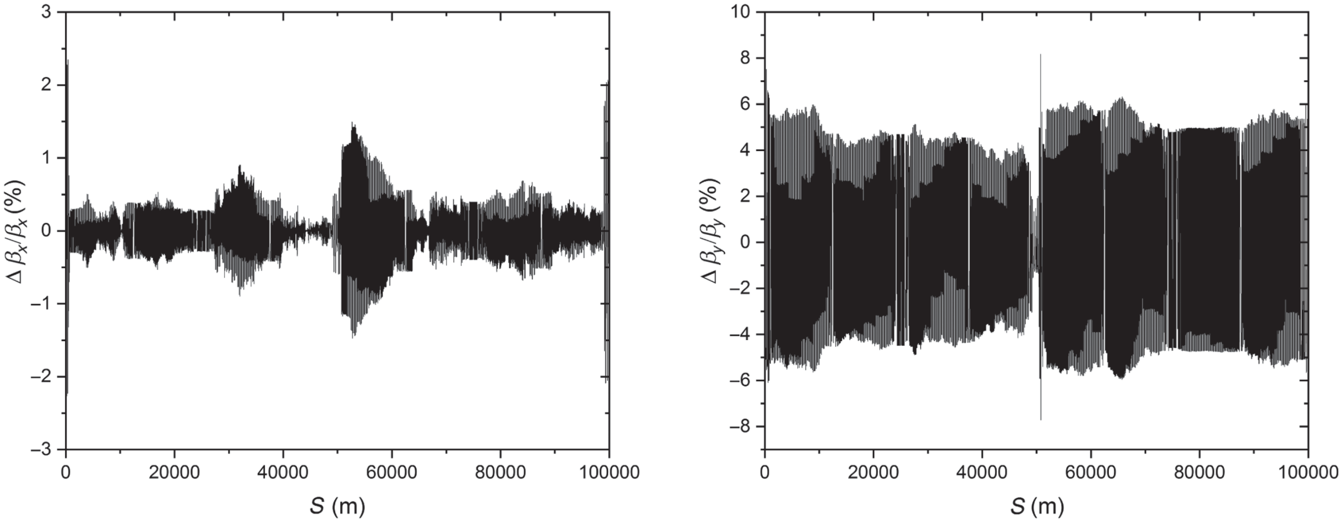

(c) Horizontal beta beating.

(d) Vertical beta beating.

FIG. 2. The closed orbit (a, b) and the beta beating (c, d) of the CEPC lattice computed by SAD at 45.6 GeV as a function of the longitudinal position S from one of the two interaction points. The rms values of the horizontal closed orbit and vertical closed orbit are 37 and 28 μm, respectively. The rms values of the horizontal beta beating and vertical beta beating are 3.6×10^{-3} and 3.4×10^{-2}, respectively. Note that in order to reduce the critical energy of synchrotron radiation from the last bending magnet upstream of each interaction point, these bending magnets are 93.4 m long. The local horizontal closed-orbit distortions are above 0.5 mm in (a) but can be reduced by implementing more orbital correctors in these regions.

The SAD version of the CEPC lattice was converted to the Bmad format using a Python script inside the Bmad package, and then a lattice file in PTC format was generated within Bmad. Previous studies [63] indicated a good match of the calculated bare lattice parameters between SAD and Bmad. The imperfect CEPC lattice was converted to the Bmad format using this Python script with minor modifications. The zero-length correctors modeled by the BEND type in SAD had to be converted to the KICKER type in Bmad. In addition, the different conventions of the rf phase and the quadrupole roll were taken into account.

Then, we compared the closed orbit and beta functions of the CEPC lattice using SAD, Bmad, and PTC, respectively. The differences are summarized in Table II. The relative difference of β function $\Delta\beta/\beta$ is defined as

$$(\Delta\beta/\beta)_{\text{code-SAD}} = \frac{\beta^1_{\text{code}} - \beta^1_{\text{SAD}}}{\beta^0_{\text{SAD}}}, \tag{49}$$

where the superscripts “0” and “1” denote the CEPC bare lattice and the CEPC imperfect lattice after the error corrections, respectively. And the subscripts “code”

TABLE II. The differences of the closed orbit (CO) and the relative difference of the beta function ($\Delta\beta/\beta$) of the CEPC at 45.6 GeV calculated by SAD, Bmad, and PTC. The minus sign indicates the difference between the two codes. "rms" is the root mean square of the difference around the ring. "MAX" means the maximum absolute value of the difference around the ring.

		$\mathrm{CO}_{\text{Bmad-SAD}}(\mathrm{m})$	$\mathrm{CO}_{\text{PTC-SAD}}(\mathrm{m})$	$(\Delta\beta/\beta)_{\text{Bmad-SAD}}$	$(\Delta\beta/\beta)_{\text{PTC-SAD}}$
Horizontal	rms	1.2×10^{-8}	9.5×10^{-8}	6.9×10^{-8}	1.6×10^{-5}
	MAX	6.8×10^{-8}	3.3×10^{-7}	9.9×10^{-8}	4.2×10^{-4}
Vertical	rms	1.4×10^{-10}	1.1×10^{-9}	9.0×10^{-7}	9.5×10^{-5}
	MAX	1.3×10^{-9}	7.8×10^{-9}	1.4×10^{-6}	6.5×10^{-4}

TABLE III. Emittances and fractional tunes of the CEPC at 45.6 GeV calculated by SAD, Bmad, and PTC.

	SAD	Bmad	PTC
Horizontal emittance (nm rad)	0.1731	0.1738	0.1733
Vertical emittance (pm rad)	1.615	1.623	1.612
Longitudinal emittance (μm rad)	0.9017	0.8956	0.9028
Fractional horizontal tune	0.108	0.108	0.108
Fractional vertical tune	0.217	0.217	0.216
Fractional synchrotron tune	0.028	0.028	0.028

represents either Bmad or PTC. For the closed orbit and the beta beating, both the rms and the maximum values of the differences in Table II are much smaller than the rms values of the lattice obtained by SAD in Fig. 2. We also compared the emittances, betatron, and synchrotron tunes using these three codes, as shown in Table III.

Although the three codes have different models, the results of simulations of the closed orbits, β functions, emittances, tunes, and other parameters match very well. The relative differences between these three codes are much smaller than the relative differences between the imperfect lattice and the bare lattice. Therefore, the simulations using Bmad and PTC can truthfully reflect the influence of the machine imperfections and the correction scheme on the CEPC lattice.

IV. APPLICATION OF THE THEORIES

In this section, we apply the theories outlined in Section II to evaluate the depolarization effects for the CEPC lattice. We first calculate the Fourier harmonics $\tilde{\omega}_k$ and $\tilde{\lambda}_k$ near the working beam energy and apply the theory of radiative depolarization taking into account spin resonances up to the first order. Then the calculated equilibrium beam polarization is compared with the simulations via the SLIM formalism. Finally, we discuss how the theories of the correlated and uncorrelated regimes are applied to evaluate the depolarization effects for the CEPC lattice.

As shown in Sec. II, the amplitudes of Fourier harmonics, $\tilde{\omega}_k$ and $\tilde{\lambda}_k$, are the major lattice-dependent inputs to the theories of depolarization effects at ultrahigh beam energies. Their evaluation only requires the closed orbit and some optical parameters that are accessible from the SAD calculations. According to the definition of the strength of the integer spin resonance in Eq. (29), $\tilde{\omega}_k$ can be approximately evaluated using

$$\begin{aligned}\tilde{\omega}_k &\approx \frac{1}{2\pi}\int_0^{2\pi R}(1+k)y_0''(s)e^{ik\Phi(s)}ds\\ &\approx \frac{1+k}{2\pi}\sum_{h=1}^{M}[p_{y,0}(s_{h,2})-p_{y,0}(s_{h,1})]e^{ik\Phi(s_{h,1})}, \qquad (50)\end{aligned}$$

where y_0 is the vertical displacement on the closed orbit and $y_0''(s)=d^2y_0(s)/ds^2$ with $ds=Rd\theta'$. We approximate $y_0'=dy_0/ds$ by $p_{y,0}$, the vertical canonical momentum on the closed orbit, and replace the integral with a sum over the M magnet elements in the lattice. $s_{h,1}$ and $s_{h,2}$ are the longitudinal positions of the entrance and the exit of the hth magnet, respectively. Similarly, $\tilde{\lambda}_k$ in Eq. (38) can be approximately calculated using

$$\begin{aligned}\tilde{\lambda}_k &= \frac{1+k}{2\pi}\int_0^{2\pi R}G_y(s)\eta_y(s)e^{ik\Phi(s)}ds\\ &\approx \frac{1+k}{2\pi}\sum_{h=1}^{M}G_y(s_{h,1})\Delta s_h\eta_y(s_{h,1})e^{ik\Phi(s_{h,1})}, \qquad (51)\end{aligned}$$

where Δs_h is the length of the hth magnet.

Figure 3 shows the $|\tilde{\omega}_k|^2$ and $|\tilde{\lambda}_k|^2$ calculated for the CEPC lattice, for various integers k near $a\gamma_0=103.5$ (corresponding to the working beam energy of 45.6 GeV). The amplitude variations are mostly within one order of magnitude. Moreover, evaluation with Eq. (40) of the rate of depolarization with just the two harmonics nearest to the integer part of $a\gamma_0$ shows that retaining just those harmonics suffices in most cases in the working energy range of the CEPC.

Then, we employed the SLIM formalism implemented in Bmad to calculate the equilibrium beam polarization as a function of $a\gamma_0$ for the CEPC lattice, centered on three working beam energies with $a\gamma_0=103.5$ (45.6 GeV, Z-pole), $a\gamma_0=181.5$ (80 GeV, WW threshold), and $a\gamma_0=272.5$ (120 GeV, Higgs), as shown in Figs. 4(a)–4(c). The step size of $a\gamma_0$ is 0.02 in the simulations. For comparison,

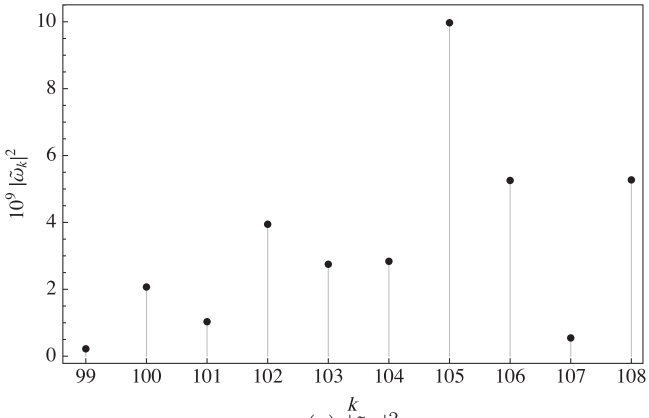

(a) $|\tilde{\omega}_k|^2$

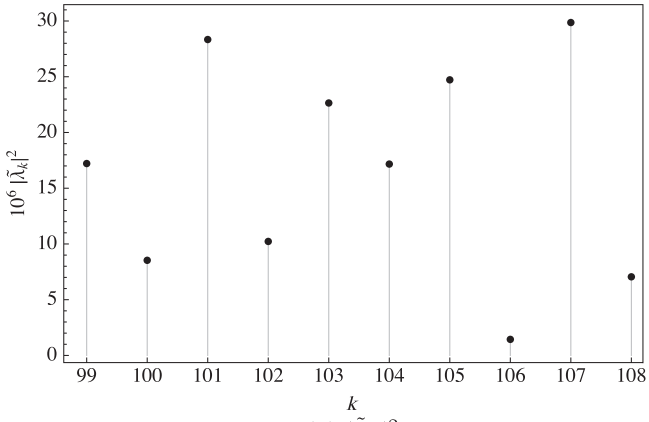

(b) $|\tilde{\lambda}_k|^2$

FIG. 3. Harmonics of $|\tilde{\omega}_k|^2$ (a) and $|\tilde{\lambda}_k|^2$ (b) near $a\gamma_0 = 103.5$ for the CEPC lattice.

we also used Eqs. (5), (10), and (40) to evaluate the equilibrium beam polarization analytically, taking into account synchrotron spin resonances up to the first order. Only the strengths of the two nearest integer spin resonances were retained in the evaluation of Eq. (40). The (numerical) SLIM simulation results match well with the analytical calculations. As the integer spin resonances in the tilt of $\hat{n}_0$ become much stronger at the working energy for the Higgs particle, the equilibrium beam polarization for the cases with $[a\gamma_0] \approx 0.5$ is also much reduced. In addition, there are dips in the equilibrium beam polarization near the first-order parent betatron spin resonances, for example, when $a\gamma_0$ is near 104 ± 0.108 at the working energy for Z. But apparently their influence is quite localized and much weaker compared to the first-order parent synchrotron spin resonances. This justifies the analysis of the relative significances of first-order spin resonances in Sec. II.

We also evaluated the depolarization effects using the theories of the correlated and uncorrelated regimes of spin resonance crossings. We used Eq. (43) to estimate the effect of the correlated resonance crossing and Eq. (48) to estimate

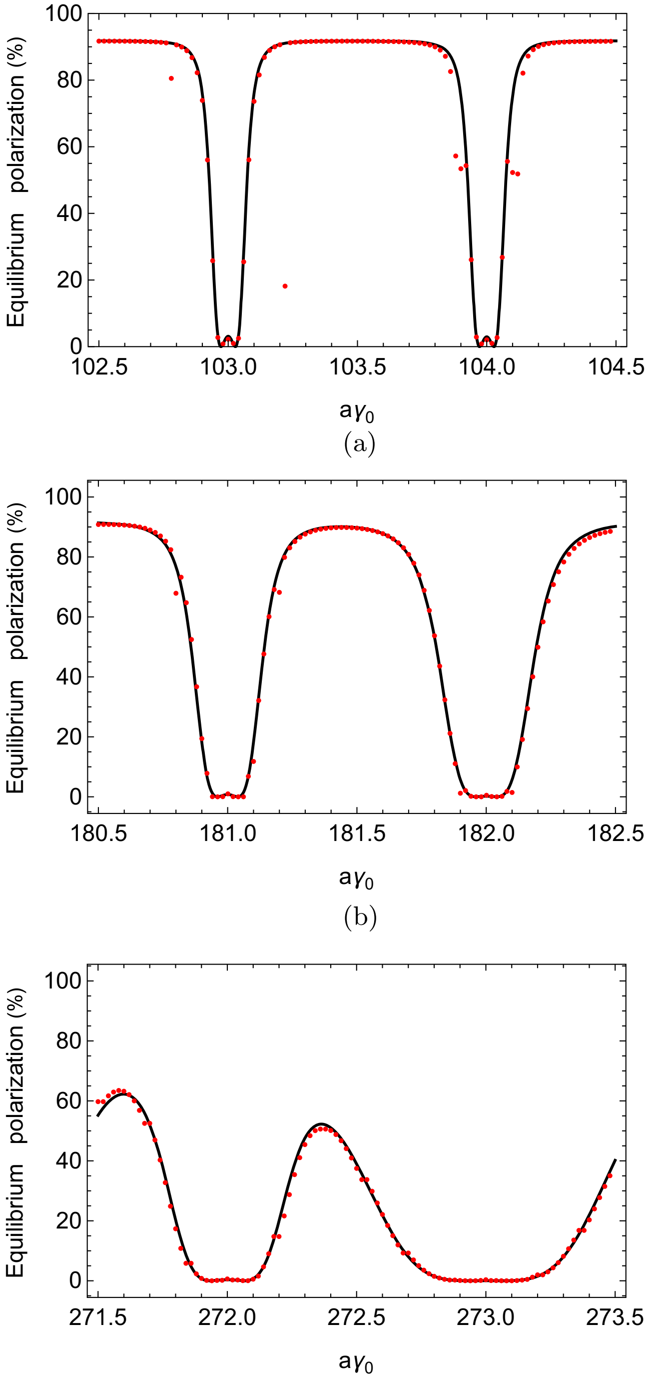

(a)

(b)

(c)

FIG. 4. The equilibrium beam polarization as a function of $a\gamma_0$ near the three working energies of the CEPC. (a) Z-pole (around 45.6 GeV), (b) WW threshold (around 80 GeV), and (c) Higgs (around 120 GeV). The red points show the simulation results of SLIM, the step size $\Delta(a\gamma_0) = 0.02$. The black curve shows the analytical calculation results using the first-order theory of Eq. (40). There are dips near first-order parent betatron spin resonances $\nu_0 \pm 0.11 = k$ (horizontal) and $\nu_0 \pm 0.22 = k$ (vertical), but these dips are much narrower compared to those around first-order parent synchrotron spin resonances.

the effect of the uncorrelated resonance crossing. Then we evaluated Eqs. (5) and (10) to estimate the equilibrium beam polarization of the CEPC lattice. In both cases, we only retained the two Fourier harmonics nearest to the integer part of $a\gamma_0$, and for Eq. (43), we retained m in the range of -100 to 100 as a result of a check of convergence.

V. RESULTS OF SIMULATIONS

In this section, we describe the evaluation of the radiative depolarization effects of the CEPC lattice using Monte Carlo simulations with the PTC code [44] and compare the results with the predictions of the theories of radiative depolarization, for various lattice settings. In the Monte Carlo simulations, a bunch of 54 particles was launched on the closed orbit with the same vertical spin and tracked for ten damping times in the presence of stochastic photon emissions but disregarding the Sokolov-Ternov effect. The decay of the beam polarization was recorded, and the data of the calculated beam polarization in the last eight damping times were fitted to obtain an estimate of the time constant of the spin diffusion τ_d. Then the equilibrium beam polarization was estimated through Eqs. (5) and (10).

A. Dependence on beam energy

We first studied the variation of the equilibrium beam polarization as a function of $a\gamma_0$ near the three operation energies, for Z, WW, and Higgs production, respectively, as shown in Figs. 5(a)–5(c). For the Z and WW energies, the valleys near integers become much wider relative to those in Figs. 4(a) and 4(b), as predicted by both theories, while the Monte Carlo simulation results agree better with the theory of the correlated regime, as the fine structure of higher-order synchrotron sideband spin resonances is clearly seen. For the Higgs energy, however, although the equilibrium beam polarization level is very low, the results of the Monte Carlo simulation are quite close to the predictions of the theory of the uncorrelated regime, but are generally higher than the prediction of the theory of the correlated regime, and there are no clear signs of higher-order synchrotron sideband spin resonances.

We then investigated the dependence of the depolarization effects on the beam energy, in the range of 45.6 to 120 GeV. The energy points were selected so that $[a\gamma_0] = 0.5$. The total rf voltage was adjusted to compensate for the increase of synchrotron-radiation energy loss at higher beam energies and the synchrotron tunes were set to the design values according to the CEPC CDR specifications at 45.6, 80, and 120 GeV. For other beam energy points, the synchrotron tunes were set in a smoothly increasing manner. The related lattice parameters are summarized in Table IV.

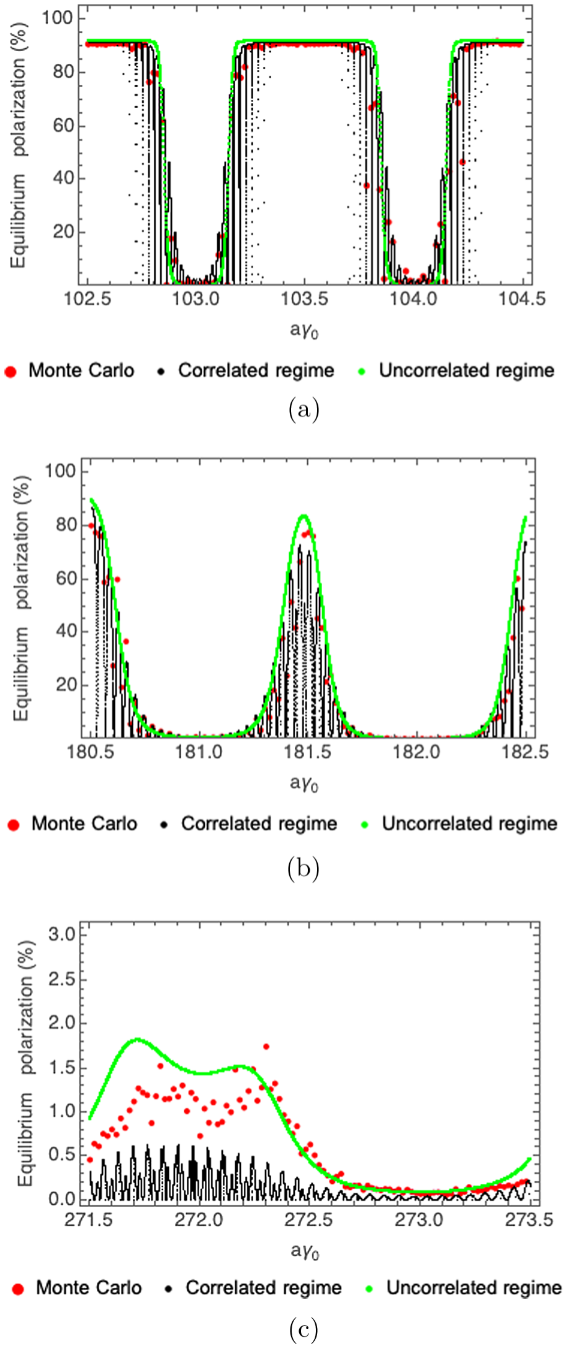

FIG. 5. The equilibrium beam polarization as a function of $a\gamma_0$ near three working energies of the CEPC. (a) Z-pole (around 45.6 GeV), (b) WW threshold (around 80 GeV), and (c) Higgs (around 120 GeV). The black dots and green dots show the equilibrium polarization calculated using the theories of correlated and uncorrelated regimes, respectively, the red points represent the Monte Carlo simulation results with a step size of $a\gamma_0$ of 0.02 in the central region. Note that in (c), a different y axis range is used since the equilibrium polarization is very low at the Higgs energy.

Figure 6(a) shows the time constant of the spin diffusion τ_d obtained by Monte Carlo simulations, the time constant of the Sokolov-Ternov effect τ_p calculated using Bmad, as well as the self-polarization buildup time τ_{tot}, at the various beam energies. τ_d decreases much faster than τ_p with increasing beam energy, as predicted by both Eqs. (43)

TABLE IV. The CEPC lattice parameters. (* indicates the planned operation energies in the CEPC CDR).

Beam energy (GeV)	$a\gamma_0$	$\lvert\tilde{\omega}_k\rvert^2$ ($\times 10^{-9}$)	$\lvert\tilde{\lambda}_k\rvert^2$ ($\times 10^{-5}$)	$\sigma_\delta(\times 10^{-4})$	ν_z	τ_p (h)	κ	σ
45.6*	103.5	$\lvert\tilde{\omega}_{103}\rvert^2 = 2.7$ $\lvert\tilde{\omega}_{104}\rvert^2 = 2.8$	$\lvert\tilde{\lambda}_{103}\rvert^2 = 2.2645$ $\lvert\tilde{\lambda}_{104}\rvert^2 = 1.7166$	3.77	0.028	252.72	0.03	1.39
60.1	136.5	$\lvert\tilde{\omega}_{136}\rvert^2 = 3.7$ $\lvert\tilde{\omega}_{137}\rvert^2 = 14.7$	$\lvert\tilde{\lambda}_{136}\rvert^2 = 0.8178$ $\lvert\tilde{\lambda}_{137}\rvert^2 = 5.5717$	4.96	0.028	63.34	0.20	2.42
69.8	158.5	$\lvert\tilde{\omega}_{158}\rvert^2 = 6.6$ $\lvert\tilde{\omega}_{159}\rvert^2 = 26.4$	$\lvert\tilde{\lambda}_{158}\rvert^2 = 0.9574$ $\lvert\tilde{\lambda}_{159}\rvert^2 = 4.4585$	5.77	0.0324	30.00	0.36	2.82
80.0*	181.5	$\lvert\tilde{\omega}_{181}\rvert^2 = 14.4$ $\lvert\tilde{\omega}_{182}\rvert^2 = 53.3$	$\lvert\tilde{\lambda}_{181}\rvert^2 = 4.9118$ $\lvert\tilde{\lambda}_{182}\rvert^2 = 15.6433$	6.61	0.0395	15.24	0.52	3.04
84.4	191.5	$\lvert\tilde{\omega}_{191}\rvert^2 = 16.3$ $\lvert\tilde{\omega}_{192}\rvert^2 = 19.8$	$\lvert\tilde{\lambda}_{191}\rvert^2 = 15.5332$ $\lvert\tilde{\lambda}_{192}\rvert^2 = 1.0088$	6.97	0.0425	11.65	0.61	3.14
90.1	204.5	$\lvert\tilde{\omega}_{204}\rvert^2 = 19.1$ $\lvert\tilde{\omega}_{205}\rvert^2 = 43.8$	$\lvert\tilde{\lambda}_{204}\rvert^2 = 3.7786$ $\lvert\tilde{\lambda}_{205}\rvert^2 = 0.6403$	7.43	0.0467	8.39	0.72	3.25
95.4	216.5	$\lvert\tilde{\omega}_{216}\rvert^2 = 15.0$ $\lvert\tilde{\omega}_{217}\rvert^2 = 34.8$	$\lvert\tilde{\lambda}_{216}\rvert^2 = 6.1547$ $\lvert\tilde{\lambda}_{217}\rvert^2 = 1.2292$	7.88	0.0515	6.31	0.80	3.31
99.8	226.5	$\lvert\tilde{\omega}_{226}\rvert^2 = 10.5$ $\lvert\tilde{\omega}_{227}\rvert^2 = 27.4$	$\lvert\tilde{\lambda}_{226}\rvert^2 = 35.2604$ $\lvert\tilde{\lambda}_{227}\rvert^2 = 4.9787$	8.24	0.0550	5.03	0.90	3.39
109.9	249.5	$\lvert\tilde{\omega}_{249}\rvert^2 = 56.9$ $\lvert\tilde{\omega}_{250}\rvert^2 = 41.3$	$\lvert\tilde{\lambda}_{249}\rvert^2 = 26.9851$ $\lvert\tilde{\lambda}_{250}\rvert^2 = 46.9963$	9.08	0.0585	3.10	1.48	3.87
120.1*	272.5	$\lvert\tilde{\omega}_{271}\rvert^2 = 770.4$ $\lvert\tilde{\omega}_{272}\rvert^2 = 95.8$ $\lvert\tilde{\omega}_{273}\rvert^2 = 1684.2$	$\lvert\tilde{\lambda}_{271}\rvert^2 = 41.6290$ $\lvert\tilde{\lambda}_{272}\rvert^2 = 12.0825$ $\lvert\tilde{\lambda}_{273}\rvert^2 = 361.7036$	9.90	0.0650	2.03	1.95	4.15

and (48) and becomes the dominant contributor to τ_{tot} at beam energies beyond 85 GeV. This leads to a much-reduced level of equilibrium beam polarization at higher beam energies, as shown in Fig. 6(b). In addition to the results derived from the Monte Carlo simulations, the calculations using the theories of the correlated and uncorrelated regimes are also presented in the figure for comparison. Up to 90 GeV, the simulated equilibrium polarization matches quite well with the theory of the correlated regime and is smaller than the theory of the uncorrelated regime. However, as the beam energies get even higher, there are nontrivial discrepancies between the results of simulations and the theories. This might suggest the paradigm shift from the correlated regime toward the uncorrelated regime. As shown previously, the results from the Monte Carlo simulation are close to the theory of the uncorrelated regime at around 120 GeV.

B. Influence of asymmetric wigglers at the Z pole

The time constant of the Sokolov-Ternov effect is as large as 253 h at the Z pole. Using the self-polarization mechanism to generate sufficient beam polarization for RD requires a much-reduced polarization build-up time. This can be achieved by implementing asymmetric wiggler magnets [19]. This possibility was investigated in detail for LEP [64] and also studied for the FCC-ee [40]. An asymmetric wiggler consists of three bending magnets. The central bending magnet has a length L_+ and a magnetic field B_+ in the same direction as the guiding magnetic field in the arcs. Its bending angle is denoted as θ_+, while the bending magnets on both sides have equal length L_-, equal magnetic field B_- in the opposite direction to B_+, and equal bending angles θ_-. It is required that $\theta_+ + 2\theta_- = 0$, ensuring no change in the layout and optics beyond the wiggler insertion. When N_w units of such asymmetric wigglers are included in the straight sections of the lattice, in addition to a decrease in τ_p, there is also a decrease in P_∞, as well as increases in synchrotron-radiation energy loss per turn, U_0, and the rms relative energy spread σ_δ. A larger σ_δ leads to a larger modulation index σ so that the higher-order synchrotron sideband spin resonances are much enhanced. This could in turn increase τ_p/τ_d and further reduce the equilibrium beam polarization level.

For the CEPC, the influence of asymmetric wigglers on radiative depolarization was evaluated quantitatively. Ten identical units of asymmetric wigglers were inserted into the straight sections of the CEPC lattice [65], with $L_- = 2$ m, $L_+ = 1$ m, i.e., $B_+/B_- = 4$. In this paper, various settings of B_+ and thus θ_+ were used to study the influence on the depolarization effects. The synchrotron tune was kept fixed at 0.028 by adjusting the total rf voltages.

Table V shows the beam parameters for the lattice without wigglers and three different wiggler settings with increasing θ_+. For example, in case 1, the time constant of the Sokolov-Ternov effect τ_p is reduced to about 32 h, and then about 2 h is needed to obtain 5% beam polarization, more or less sufficient for energy calibrations. Cases 2 and 3 use even stronger wiggler magnets, and the increase in U_0

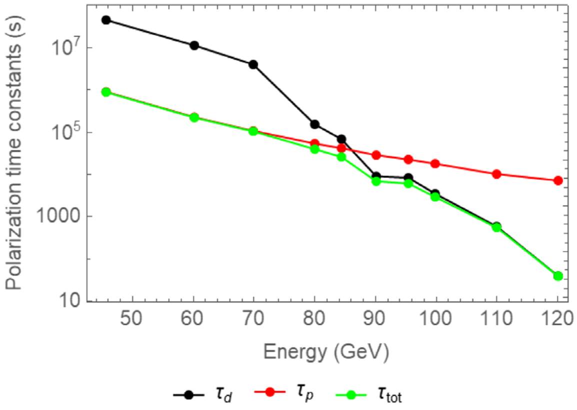

(a) Polarization time constants

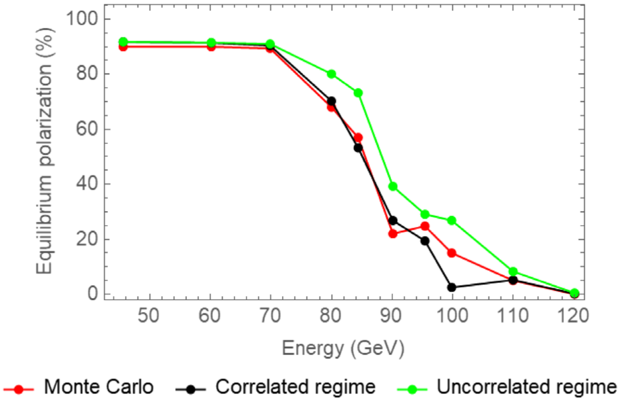

(b) Equilibrium beam polarization

FIG. 6. Polarization time constants (a) and equilibrium beam polarization (b) as a function of beam energies for the CEPC lattice. In (b), estimates of the equilibrium beam polarization using the theories of "correlated regime" and "uncorrelated regime" are also plotted for comparison with those derived from the Monte Carlo simulations.

and σ_δ is more substantial. Though not relevant for practical use, these cases are employed here out of academic interest. In these three cases, and as depicted in the plots of equilibrium beam polarization in Fig. 7, the locations of higher-order synchrotron sideband spin resonances are kept the same while the theory of the correlated regime predicts lower levels of equilibrium polarization and wider valleys near these resonances for increasing wiggler strengths characterized by θ_+. In contrast, as predicted by the theory of the uncorrelated regime, there are no higher-order synchrotron sideband spin resonances and the equilibrium polarization level is higher for $a\gamma_0$ near 103.5 compared to the prediction of the theory of the correlated regime.

As shown in Fig. 7, the Monte Carlo simulation results are compared with the theories of the correlated regime and the uncorrelated regime. Figure 7(a) shows the outcomes of case 1 where the Monte Carlo simulation results fit well with the theory of the correlated regime, with obvious polarization dips in the synchrotron-sideband spin resonance regions, which are absent in the theory of the uncorrelated regime. Figure 7(b) shows the outcomes of case 2 where the results of the Monte Carlo simulation are inconsistent with the valleys predicted by the theory of the correlated regime. Figure 7(c) shows the outcomes of case 3 where the results of Monte Carlo simulations show no obvious resonance structures and are generally between the predicted levels of equilibrium beam polarization of the two theories.

These results of the Monte Carlo simulations indicate deviations from the theory of the correlated regime, when the condition $\kappa \ll 1$ on the correlation index no longer holds, but are not in agreement with the theory of the uncorrelated regime either. Using even larger θ_+ in the lattice setup leads to an rf bucket insufficient for fully capturing the beam particles in the simulations and thus this parameter space was not explored.

In addition, we fixed the beam energy at 45.6 GeV and scanned θ_+ to study the dependence of the energy loss per turn, rms relative energy spread, polarization time, and equilibrium polarization, as shown in Fig. 8. The results of simulations for the equilibrium polarization match well with the theory of the correlated regime for small θ_+ settings. However, there is an increasing deviation for θ_+ larger than 0.004 rad. In the parameter range covered, the results of the Monte Carlo simulations are between the equilibrium polarization levels predicted by the two theories, respectively.

TABLE V. Beam parameters for various wiggler settings.

wigglers	θ_+ (rad)	U_0 (MeV)	σ_δ ($\times 10^{-4}$)	τ_p (h)	κ	σ
w/o	0	36.1	3.77	252.8	0.03	1.39
Case 1	0.0033	43.9	9.53	32.3	0.22	3.52
Case 2	0.0056	60.0	17.26	7.2	1.00	6.38
Case 3	0.0080	84.8	24.55	2.5	2.85	9.07

C. Influence of rf settings at the Z pole

In the CDR for the CEPC, it is assumed that the ring has a single-frequency rf system of 650 MHz. Then, for a chosen momentum compaction factor, e.g., according to Eqs. (3.43) and (5.66) in Ref. [66], the bunch length and synchrotron tune cannot be adjusted separately. However, earlier studies revealed a novel coherent head-tail instability (X-Z instability) induced by the beam-beam interaction at a large Piwinski angle [67,68], which could be enhanced when the longitudinal impedance is also taken into account [69,70]. Thus, it was suggested [71] that the instability could be viably mitigated by including a higher-harmonic rf system to lengthen the bunches. It has also been suggested that bunch lengthening can lead to a reduction in the center-of-mass energy spread in e^+/e^- collisions. For noncolliding bunches, the introduction of the harmonic cavity itself does not help to reduce the rms energy spread. However, for colliding bunches, the rms

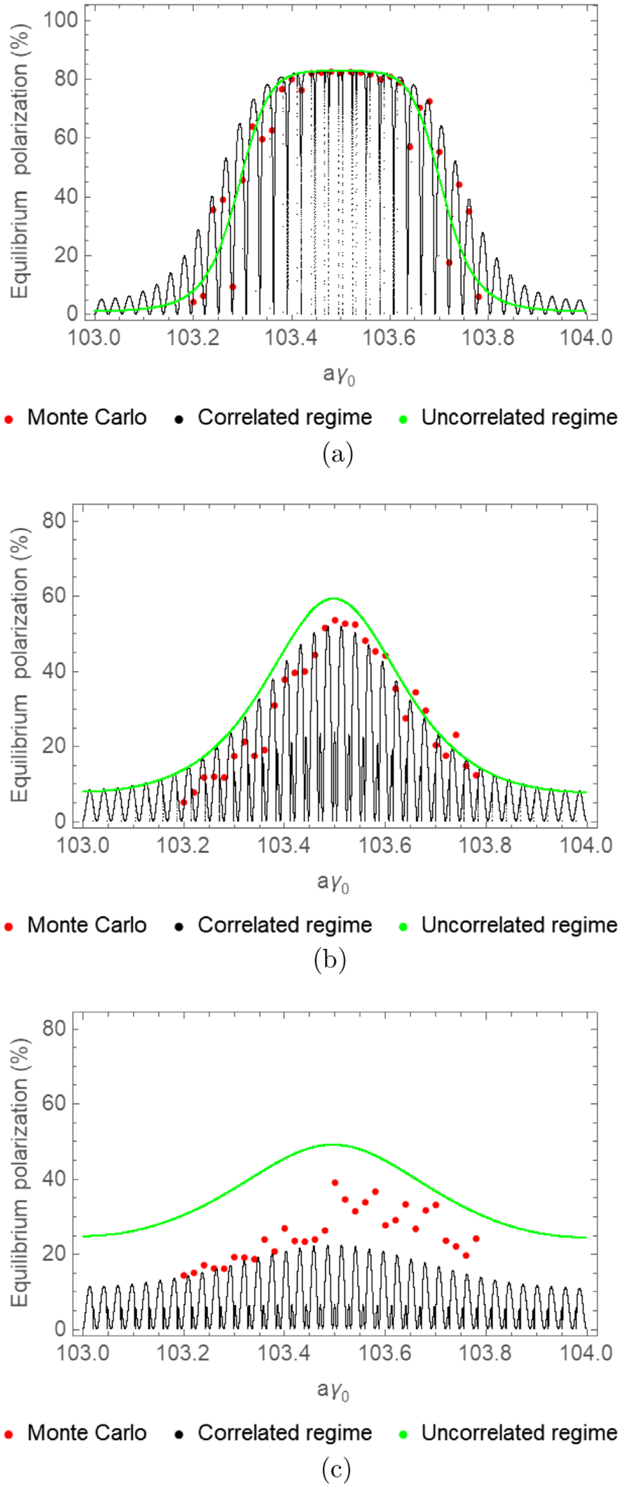

FIG. 7. The equilibrium polarization vs spin tune for the CEPC lattice in the presence of ten wigglers. The Monte Carlo simulations adopt a step size of $a\gamma_0$ of 0.02. (a) Case 1: $\theta_+ = 0.0033$ rad. (b) Case 2: $\theta_+ = 0.0056$ rad. (c) Case 3: $\theta_+ = 0.0080$ rad.

energy spread of a beam can suffer from a significant increase due to beamstrahlung and the beamstrahlung-induced energy spread can to some extent be alleviated by the introduction of harmonic cavities [72]. Of course, a reduction of the rms energy spread in the beams also reduces the spread in the instantaneous spin-precession rate.

In such a double rf system, the synchrotron tune ν_z at zero amplitude is different from that of a single rf system and so is the dependence of ν_z on the synchrotron amplitude [73,74]. Since both the modulation index σ and the correlation index κ depend on ν_z, it is expected that the radiative depolarization effects can be different.

Although there is currently no plan to use a double rf system for the CEPC, a study of the effect of radiative depolarization with such a system opens up new directions for study which might bare fruit in the future. We, therefore, now look in detail at the effects of a double-frequency system for the CEPC running near 45.6 GeV.

Simulations with the thick-lens SLIM algorithm in the code SLICKTRACK [30] for a real ring show that synchrotron motion for a single rf system is close to simple harmonic although the rf cavities are localized. Then it is reasonable, as a first step, to follow the description in Ref. [74] in which the rf system is distributed uniformly. Moreover, only synchrotron motion is included here but the applicability of this model has been confirmed *a posteriori* with Monte Carlo simulations with localized cavities as described below.

Thus we begin by writing the voltage seen by beam particles in the presence of a double-frequency rf system as

$$V_{\mathrm{tot}}(\phi) = V_1 \sin(\phi + \phi_{s1}) + V_2 \sin(n\phi + \phi_{s2}), \tag{52}$$

where ϕ is the rf phase of a particle relative to that of the reference particle, V and ϕ_s are the total voltage, and rf synchronous phase for each rf frequency, with subscripts "1" and "2" denoting the fundamental and the harmonic rf system, respectively, and the integer n is the ratio of the harmonic rf frequency to the fundamental rf frequency. The parameters of the double-frequency rf system must be set to compensate for the synchrotron-radiation energy loss per turn U_0, this requires

$$eV_1 \sin(\phi_{s1}) + eV_2 \sin(\phi_{s2}) = U_0, \tag{53}$$

where e is the charge of the electron.

There are still 3 degrees of freedom in the parameters of the double rf system. To simplify the discussion in this paper, we study three different cases of rf settings. All these cases feature a single rf bucket and beam particles oscillate around a single "stable" fixed point at $(z, \delta) = (0, 0)$. In case A, we set $V_2 = 0$ MV so that the double rf system effectively reduces to the case of the single rf system. Then we specify V_1 as the only independent variable, which is related to the rms bunch length and the rf bucket height. In case B, we fix $\phi_{s2} = 0$ rad so that $eV_1 \sin(\phi_{s1}) = U_0$, and thus with Eq. (53), the settings of the fundamental rf system are the same as that of a single rf system alone. For a specified V_1, we choose various positive values of V_2 that lead to different rms bunch lengths and different

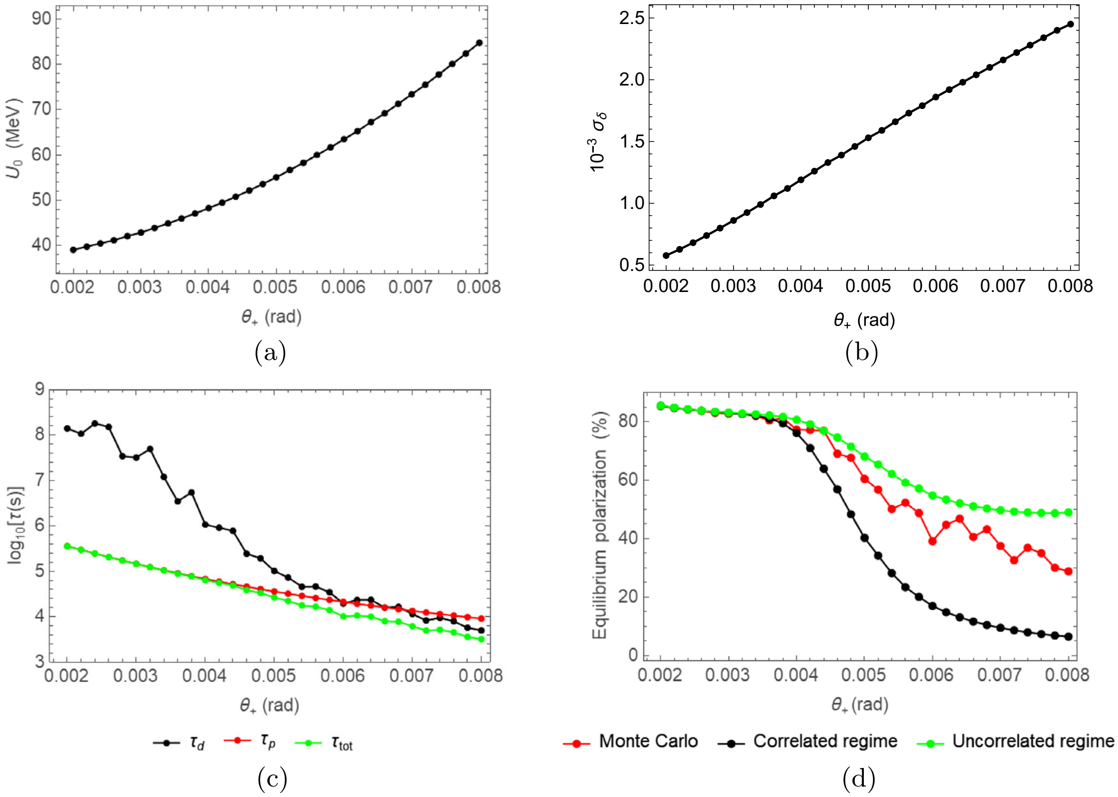

(a) (b)

(c) (d)

FIG. 8. The energy loss per turn, rms relative energy spread, polarization time, and equilibrium polarization vs θ_+. The step size $\Delta\theta_+ = 0.0002$ rad. (a) U_0 vs θ_+. (b) σ_δ vs θ_+. (c) Polarization time constants vs θ_+. (d) $P_{\rm eq}$ vs θ_+.

dependences of synchrotron tune on the synchrotron amplitude. Note that this reduces to case A if $V_2 = 0$ MV. In case C, we consider a special type of setting called the "ideal bunch lengthening" condition, with a vanishing slope of the rf wave at the synchronous phase. This requires both the first and second derivatives of the total rf voltage at the synchronous phase to be set to zero [73]:

$$\left.\frac{\partial V_{\rm tot}}{\partial\phi}\right|_{\phi=0} = 0$$
$$\left.\frac{\partial^2 V_{\rm tot}}{\partial\phi^2}\right|_{\phi=0} = 0 \tag{54}$$

so that

$$V_2 = \sqrt{\frac{V_1^2}{n^2} - \frac{U_0^2}{n^2-1}}$$
$$\phi_{s1} = \pi - \arcsin\left(\frac{n^2}{n^2-1}\frac{U_0}{V_1}\right)$$
$$\phi_{s2} = -\arcsin\left(\frac{1}{n^2-1}\frac{U_0}{V_2}\right). \tag{55}$$

We specify V_1 as the only independent variable, all other rf parameters are determined using Eq. (55).

In the following studies, we use the CEPC lattice with the wiggler settings of case 1 and consider a fundamental rf system running at 650 MHz and a harmonic rf system running at 1.3 GHz.

But before describing our numerical results for the three different cases of rf settings, we direct the reader to the Appendix (Sec. A 3) where the mathematical details are presented together with illustrative plots of the regions of stable motion in δ and ϕ and indications of the positions of the unstable fixed points and the turning points. Then, with that formalism, we evaluate the synchrotron tune ν_z at various synchrotron amplitudes as well as the equilibrium longitudinal distribution $\rho(z)$ of particles under the influence of damping and excitation by synchrotron radiation. For that, we choose a beam energy of 45.72 GeV ($a\gamma_0 = 103.76$) and fix $V_1 = 103.372$ MV. Then $\phi_{s1} = 2.693$ rad in cases A and B. For case C, $\phi_{s1} = 2.526$ rad, $V_2 = 44.750$ MV, and $\phi_{s2} = -0.340$ rad.

The dependences of ν_z on the orbital amplitudes of the three cases are shown in Fig. 9(a) where, as indicated in the Appendix (Sec. A 3), the amplitudes are represented by the measure z_{H_0}. As shown, a larger V_2 in case B leads to a lower ν_z at zero synchrotron amplitude relative to that of case A and approaches a vanishing ν_z at zero synchrotron amplitude in case C. The latter is expected given that, as mentioned earlier, the slope of the rf wave is zero at the synchronous phase. In addition, ν_z is essentially proportional

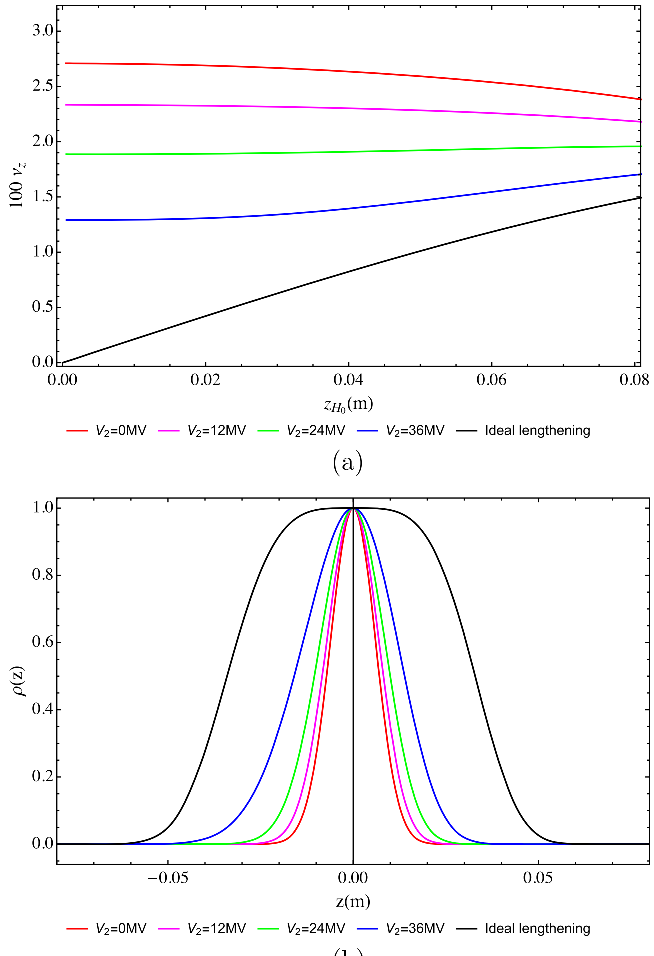

(a)

(b)

FIG. 9. The dependence of the synchrotron tune ν_z on the synchrotron amplitude, and the longitudinal distribution $\rho(z)$ of beam particles, for various settings of a double rf system. The beam energy is set to 45.72 GeV ($a\gamma_0 = 103.76$) and $V_1 = 103.372$ MV. The red curves correspond to case A with a single rf system alone, the magenta, green and blue curves correspond to three instances of case B with $\phi_{s2} = 0$ rad but different V_2, and the black curves correspond to case C at the ideal lengthening condition. (a) Amplitude dependent synchrotron tune. (b) Beam longitudinal distribution.

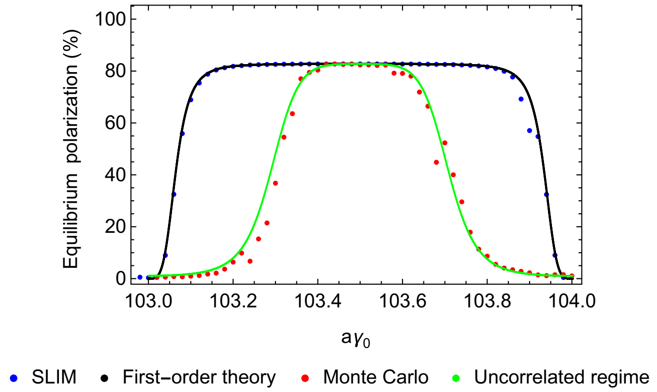

FIG. 10. The equilibrium polarization for the CEPC with the wiggler setting case 1 and the double rf system under the ideal lengthening condition.

to the amplitude of z at a small amplitude in case C and the spread of ν_z among beam particles is much larger compared to that of cases A and B. As shown in Fig. 9(b), the longitudinal distribution $\rho(z)$ in the presence of damping and synchrotron radiation is Gaussian in case A and features a flattop and a much wider distribution in case C. The distribution $\rho(z)$ becomes wider for increasing V_2 in case B and falls between the distributions of cases A and C. In addition, if we choose an even larger V_2 (for example, 50 MV) in case B, then $(z, \delta) = (0, 0)$ is no longer a single stable fixed point that beam particles oscillate around. Instead, there are two stable fixed points within the single rf bucket so that the longitudinal distribution follows a "double-hump" shape, and the distribution of ν_z in terms of z would be more complicated. This "over-stretched" regime is discussed in Ref. [74] but is beyond the scope of this paper.

The applicability of the model with a uniform distribution of the rf system is illustrated in the Appendix (Sec. A 3) where one sees good agreement for case C between the predictions of the model and the distributions in δ and z from Monte Carlo simulations with the two kinds of localized cavities and full synchrobetatron motion.

Now we are ready to present the influence of the various settings of the double rf system on the radiative depolarization effects. For case A with a single rf system alone, the results of equilibrium polarization for the CEPC have already been shown in Fig. 7(a). Although different settings of the rf voltage and phase were used relative to those of case A in Fig. 9, the Monte Carlo simulation results agree with the prediction of the theory of the correlated regime.

For case C at the ideal bunch lengthening condition, as already shown in Fig. 9(a), the synchrotron tune ν_z is zero at zero amplitude. A direct application of Eq. (41), by plugging $\nu_z = 0$ at zero amplitude, then leads to a vanishing enhancement factor so that the expected equilibrium beam polarization of the theory of the correlated regime is the same as the result of the first-order theory. Meanwhile, the correlation index κ is infinite and it is expected that the theory of the uncorrelated regime is applicable.

We chose a beam energy of 45.6 GeV and selected the following parameters of the double rf system to match the ideal bunch lengthening condition: $V_1 = 112.217$ MV, $\phi_{s1} = 2.592$ rad, $V_2 = 50.047$ MV, and $\phi_{s2} = -0.297$ rad. To simplify the treatment, this rf setting was used in the simulations at different beam energies in the range of $a\gamma_0 = 103$ to $a\gamma_0 = 104$. Then the "ideal bunch lengthening" condition is exactly met for $a\gamma_0 = 103.5$, with minor deviations for other beam energies. Figure 10 shows the equilibrium beam polarization for the CEPC. On one hand, the results of SLIM calculations with equal numbers of both kinds of localized cavities match well with the prediction of the first-order theory. On the other hand, the results of Monte Carlo simulations are in good agreement with the predictions for the theory of the uncorrelated regime and are quite different from the predictions of the first-order theory. These results are indeed consistent with the theory of the uncorrelated regime encapsulated in Eq. (48).

We also studied the influence of the double rf settings in case B on the radiative depolarization effects. Here, we fixed the beam energy at $E = 45.72$ GeV ($a\gamma_0 \approx 103.76$), where there is a more obvious contrast in the behavior of the equilibrium beam polarization. We fixed the settings at $V_1 = 103.372$ MV, $\phi_1 = 2.693$ rad, and $\phi_2 = 0$ and scanned the total voltage of the harmonic rf system V_2 from 0 to 45.07 MV, thus obtaining a range of synchrotron tunes at zero amplitude of synchrotron motion, from 0.028 down to 0.005.

The outcome is shown in Fig. 11 where the equilibrium beam polarization is plotted as a function of the synchrotron tune at zero amplitude and the results of the Monte Carlo simulation are compared with the predictions of the theories. The theory of the uncorrelated regime encapsulated in Eq. (48) predicts that the equilibrium beam polarization is independent of the synchrotron tune, in strong contrast with the prediction of the theory of the correlated regime, whereby a closer examination of Eq. (43) indicates that the equilibrium beam polarization should oscillate as the distance to the nearest higher-order synchrotron sideband spin resonance varies with ν_z at zero amplitude. Thus, the dips correspond to certain higher-order synchrotron sideband spin resonances and as ν_z at zero amplitude increases, so does the distance between adjacent dips (and adjacent peaks), as well as the peak equilibrium beam polarization. The results of the Monte Carlo simulation match well with the theory of the correlated regime for ν_z at zero amplitude larger than 0.025 and are in-line with the theory of the uncorrelated regime for ν_z at zero amplitude smaller than 0.01. Between these two extremes, the simulation results suggest a transition from the correlated regime to the uncorrelated regime. The vertical dashed line corresponds to $\kappa = 1$ to guide the eye, but we cannot detect a clear boundary between the correlated regime and the uncorrelated regime.

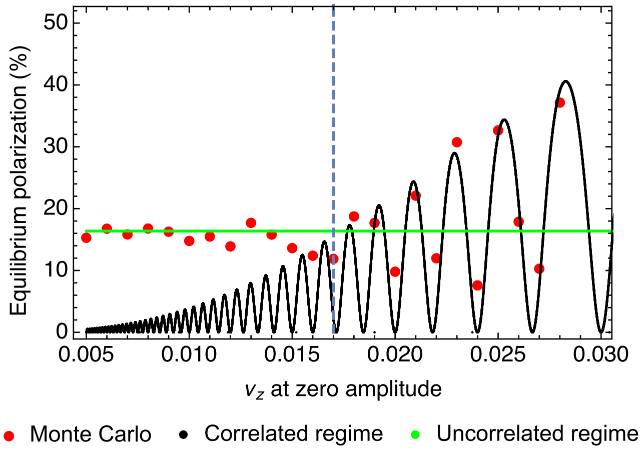

FIG. 11. The equilibrium polarization vs synchrotron tune at zero amplitude for the CEPC lattice with the wiggler setting case 1 at $a\gamma_0 \approx 103.76$. The blue dashed line corresponds to the condition $\kappa = 1$. We chose a step size of $\Delta\nu_z = 0.001$ in the Monte Carlo simulations.

In summary, when the synchrotron tune at zero amplitude is very small, in the presence of a harmonic rf system, the Monte Carlo simulation results agree well with the theory of the uncorrelated regime. As the synchrotron tune at zero amplitude becomes larger, the Monte Carlo simulations indicate a gradual transition from the uncorrelated regime to the correlated regime and match well with the theory of correlated regime when $\kappa \ll 1$.

As we already mentioned in Sec. II B, the theory of the correlated regime was derived under the assumption that the synchrotron motion is approximately harmonic, which is applicable in case A. However, in the presence of a double-rf system, the synchrotron motion could become nonlinear even at small amplitudes. This is particularly true in case C. In case B, as we increase the voltage of the harmonic rf system V_2, the synchrotron motion at small amplitudes becomes more nonlinear and deviates from case A. However, the nonlinear synchrotron motion of ϕ and δ can still be represented by action-angle variables, but in a much more complicated form involving elliptical functions [74]. It is unclear whether simple analytical forms for $\partial\hat{n}/\partial\delta$ like those underlying Eq. (43), can be obtained following the approach of derivation in Ref. [45] in this context. However, it is clear that the application of the theory of correlated regime is limited to the case where the assumption of approximately harmonic synchrotron motion is still valid.

VI. SUMMARY, CONCLUSIONS, COMMENTARY, AND FUTURE NUMERICAL WORK

This paper presents a detailed investigation of the radiative depolarization effects in the CEPC. Both theoretical evaluations and Monte Carlo simulations are employed and compared, for a CEPC CDR lattice with detailed error modeling and after dedicated corrections, and for various lattice settings.

The contribution from the first-order parent synchrotron spin resonances to radiative depolarization is explicitly derived and its connection to the underlying integer spin resonance strengths is established, for ultrahigh energy electron storage rings. This agrees with the expressions in Ref. [19] for a vanishing synchrotron tune. SLIM simulations for the CEPC lattice agree well with this first-order theory for various beam energies and also indicate that the first-order parent betatron spin resonances are much weaker compared to the first-order parent synchrotron spin resonances.

There are two distinct theories [19] that describe the influence of synchrotron oscillations on radiative depolarization at ultrahigh beam energies. The theory of the correlated regime highlights the enhancement of the parent spin resonances by higher-order synchrotron sideband spin resonances, while the theory of the uncorrelated regime predicts vanishing resonance structures and a generally higher equilibrium beam polarization level compared to the theory of the correlated regime. Monte Carlo simulations have been conducted for various beam energies, various settings of asymmetric wigglers at the Z energy, as well as for various settings of harmonic rf cavities. On one hand, these simulation results are in-line with the theory of the correlated regime for a correlation index $\kappa \ll 1$. On the other hand, the simulation results of the double-rf system in the ideal lengthening condition are consistent with the theory of the uncorrelated regime, while κ is infinite by definition. Between these two extremes, the Monte Carlo simulations of the equilibrium beam polarization are generally between the predictions of these two theories but are not in line with either. This indicates a gradual evolution from the correlated regime to the uncorrelated regime.

Then we can state our conclusions as follows: These analyses supplement previous studies that focused on theoretical aspects and numerical estimates in assessing the effects of radiative depolarization in future ultrahigh energy electron storage rings. In particular, the comparison between the results of our Monte Carlo simulations and those of the theories suggests that radiative depolarization can be reasonably estimated by evaluations of the spin-resonance strengths and use of theoretical formulas in certain parameter regions, before conducting time-consuming but more reliable Monte Carlo simulations. On the other hand, these studies also suggest that known theories of radiative depolarization are still incomplete.

We thus suggest that further theoretical investigations are required in order to to achieve a more complete description of radiative depolarization, which merges into these two theories at extremes. In that context, we make the following observations. Electron and positron storage rings need accelerating cavities in order to replace the particle energy lost by synchrotron radiation. Then the particle dynamics is unavoidably intrinsically time dependent and that is recognized in [20,21,45,75] among many others. Thus, for example, the vector $\hat{n}$ of the ISF is a function of all six canonical orbital variables as well as θ. Moreover, as in [38], it can be argued that for phase-space equilibrium and for the relatively slow variation of the polarization, the local polarization vector $\vec{P}_{\mathrm{loc}}(\vec{u};\theta)$ at each point in six-dimensional phase space is parallel to $\hat{n}(\vec{u};\theta)$ defined on six-dimensional phase space. This is the so-called ISF approximation. However, the ISF in [16,19] is defined to be explicitly time independent. Then in [19], synchrotron motion is added to the dynamics by hand. So what, then, is the direction of $\vec{P}_{\mathrm{loc}}(\vec{u};\theta)$ at orbital equilibrium in that case? In any case, we expect the ISF approximation to apply in the regime of nonresonant spin diffusion but it perhaps needs verification for the regime of resonant spin diffusion. Moreover, if the ISF is not relevant in the regime of resonant spin diffusion, what is the status of the terms $[1 - \frac{2}{9}(\hat{n} \cdot \hat{s})^2]$ and $\hat{b} \cdot \hat{n}$ in the DK formula, Eq. (7)? Should the averages involving $\hat{n}$ in those terms simply be replaced by averages involving $\hat{n}_0$ as is usually done anyway in practical evaluations of the depolarization-free asymptotic polarization?

Fortunately, we can now evaluate the validity of the theory behind resonant spin diffusion and uncorrelated resonance crossing at ultrahigh energy by following the history of individual spins using Monte Carlo simulations. So ν_0 could be set close to, or far away, from resonances and the effects on single spins of large synchrotron amplitude or large photon energy could be studied in detail and perhaps then used to predict the behavior of ensembles.

Monte Carlo codes like Bmad can also be used to check and support analytical calculations. For example, it has been seen that some perturbative calculations involving $\partial\hat{n}/\partial\delta$ of the rate of depolarization for nonresonant spin diffusion do not always converge at high energy as more and more synchrotron sidebands are included [57,59]. Then Monte Carlo simulations should be used instead. Of course, this matter is unrelated to the smoothing away of synchrotron sidebands in the regime of uncorrelated resonance crossing.

It should be noted that the so-called Bloch equations [37–39] foreseen in [21] have the potential to expose deviations from the DK formula, Eq. (7), starting from first principles.

Under the heading of future numerical work, we are aware of developments in Bmad, in particular, its facility to gain speed by using preestablished spin-orbit maps [76] for tracking between dipoles where radiation takes place, instead of tracking element-by-element. The increase in computing speed provided by this advanced feature, so-called "sectioning," should make it possible in future studies to track many more particles, launch finer parameter scans while simulating the resonant-depolarization process.

The results presented here refer to a single set of error seeds. Future work, facilitated by sectioning, will employ several sets of error seeds in order to obtain a better overview. For example, ensembles of distortions of $\hat{n}_0$ and deviations of ν_0 from $a\gamma_0$ will be available. The statistical spread of ν_0 due to closed-orbit distortions will give insights into how well the beam energy, and then the center-of-mass energy, can be estimated with RD [77]. In addition, more contributors to depolarization like the detector solenoids, the spin rotators needed to realize longitudinal polarization and more complete sources of machine imperfections, shall be included in future studies. These are important for predicting the attainable beam polarization level and for establishing methods for realizing a high beam polarization. Note that we did not implement dedicated corrections such as in harmonic closed-orbit spin matching schemes [54,55], which decrease the distortion of

$\hat{n}_0$. Applications of these correction schemes shall be carefully studied in order to optimize the attainable beam polarization, as part of an integrated approach to performance optimization in these future colliders.

We finish by reiterating some points already mentioned above. So new work is needed to provide a firm theoretical basis to bring predictions of theory and simulations more in line and future simulations will be made for more lattice seeds with more extensive sources and corrections of machine imperfections and with many more particles.

ACKNOWLEDGMENTS

W. X. would like to thank S. Nikitin and F. Meot for their early guidance in spin dynamics studies. The authors are grateful to D. Sagan and E. Forest for their kind help with BMAD/PTC. The authors acknowledge the proofreading and suggestions of S. Nikitin. D. P. B. thanks K. Heinemann and J. A. Ellison for collaboration on many aspects of spin dynamics. This study was supported by National Key R&D Program of China (Grants No. 2018YFA0404300 and No. 2016YFA0400400); National Natural Science Foundation of China (Grant No. 11975252); Key Research Program of Frontier Sciences, CAS (Grant No. QYZDJ-SSW-SLH004); Youth Innovation Promotion Association CAS (No. 2021012).

APPENDIX

1. The calculation of $\vec{e}_y \cdot \hat{k}_0$

$\hat{k}_0$ can be expanded in terms of $\hat{n}_{00}$, $\hat{k}_{00}$, and $\hat{k}_{00}^\star$ as

$$\hat{k}_0 \approx \hat{k}_{00} + c_1\hat{n}_{00} + c_2\hat{k}_{00} + c_3\hat{k}_{00}^\star, \tag{A1}$$

where $|c_1|^2 + |c_2|^2 + |c_3|^2 \ll 1$. In fact, it can be shown that $c_3 = 0$ due to the orthonormality of $\hat{m}_0$ and $\hat{l}_0$. Consider that $\hat{k}_{00}$ is in the horizontal plane, while $\hat{n}_{00} \| \vec{e}_y$,

$$\vec{e}_y \cdot \hat{k}_0 \approx c_1. \tag{A2}$$

Putting Eq. (A1) into the Thomas-BMT equation [Eq. (2)] on the closed orbit, we find

$$\frac{\partial c_1}{\partial \theta}\hat{n}_{00} = \Delta\vec{\Omega} \times \hat{k}_0 = i\Delta\vec{\Omega} \cdot \hat{k}_{00} \tag{A3}$$

then the solution of c_1 is

$$\begin{aligned} c_1 &\approx \operatorname*{Lim}_{\epsilon\to+0}\left[i\int_{-\infty}^{\theta} e^{\epsilon\theta'}\Delta\vec{\Omega}\cdot\hat{k}_{00}(\theta')d\theta'\right] \\ &\approx \operatorname*{Lim}_{\epsilon\to+0}\left[i\int_{-\infty}^{\theta} e^{\epsilon\theta'}\Delta\Omega_x e^{i\nu_0\Phi(\theta')}d\theta'\right]. \end{aligned} \tag{A4}$$

Here $\Phi(\theta') = R\int_0^{\theta'}\frac{1}{\rho_x}d\theta''$. $\Delta\Omega_x$ is the component of $\Delta\vec{\Omega}$ along the x direction and represents the influence of the radial magnetic field.

Then, the integrand of Eq. (A4) can be expanded into Fourier series,

$$\Delta\Omega_x e^{i\nu_0\Phi(\theta')} = \sum_{k=-\infty}^{\infty}\tilde{\omega}_k e^{i(\nu_0-k)\theta'}. \tag{A5}$$

where $\tilde{\omega}_k$ is the complex strength of the integer spin resonance,

$$\tilde{\omega}_k = \frac{1}{2\pi}\int_0^{2\pi}\Delta\Omega_x e^{i\nu_0(\Phi(\theta')-\theta')+ik\theta'}d\theta'. \tag{A6}$$

Equation (A4) can be simplified to the following form:

$$\vec{e}_y\cdot\hat{k}_0(\theta) \approx i\sum_{k=-\infty}^{\infty}\frac{\tilde{\omega}_k e^{i(\nu_0-k)\theta}}{\nu_0-k}. \tag{A7}$$

Note that the denominators in this expression are an artifact of the approximations used here and that this expression must be used with care when ν_0 is near an integer to avoid invalidating the approximations.

2. ξ_j of an ultrahigh energy electron storage ring

The Fourier harmonic ξ_j of the vertical component of $\vec{\omega}_z$ is

$$\xi_j = -\frac{1+a\gamma_0}{2\pi}\int_0^{2\pi}R\eta_x G_x e^{ij\theta}d\theta. \tag{A8}$$

Let us consider an ultrahigh-energy electron storage ring lattice composed of P superperiods, where each superperiod contains a straight section with a length L_{ss} which is dispersion free, and an arc including M FODO cells with half-length L with the following structure [QF/2 B QD B QF/2].

Then, following the treatment of Lee [50], the Fourier harmonic ξ_j becomes

$$\begin{aligned} \xi_j \approx &-\frac{1+a\gamma_0}{2\pi}\left[\frac{\eta_{QF,x}}{f_{QF}}\cos\left(j\frac{L}{R}\right)+\frac{\eta_{QD,x}}{f_{QD}}\right] \\ &\times\varsigma\left(P,\frac{j}{P}\right)\varsigma\left[M,\frac{j}{MP}\left(1-\frac{PL_{\mathrm{ss}}}{2\pi R}\right)\right] \\ &\times e^{ij\frac{L+L_{\mathrm{ss}}}{R}}e^{ij\frac{P-1}{P}\pi}e^{ij\frac{M-1}{MP}\pi(1-\frac{PL_{\mathrm{ss}}}{2\pi R})}, \end{aligned} \tag{A9}$$

where the enhancement function $\varsigma(N,x)$ is given by

$$\varsigma(N,x) = \frac{\sin(N\pi x)}{\sin(\pi x)} \tag{A10}$$

and where N is a positive integer and $x \in \mathbb{R}$. Figure 12 shows $\varsigma(N,x)/N$ for several different N. The following are

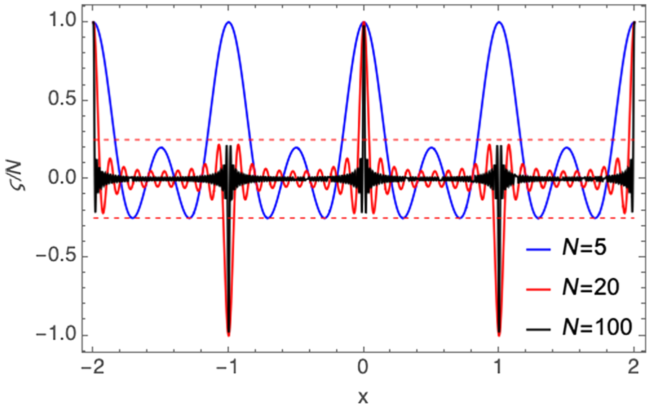

FIG. 12. The enhancement function $\varsigma(N,x)$ for various N. The red dashed lines indicate $|\varsigma/N| = 1/4$ as a reference.

some key properties of $\varsigma(N,x)$. (i) $\varsigma(N,x) = 0$ when $N * x \in \mathbb{Z}$ while $x \notin \mathbb{Z}$; (ii) $|\varsigma(N,x)| \to N$, as x approaches an integer k; and (iii) for $N \geq 5$, $|\varsigma(N,x)| \leq \frac{N}{4}$ for $|x-k| \geq \frac{0.8}{N}$, where k is the integer nearest to x.

Taking the thin-lens approximation, the dispersion functions at the center of the focusing quadrupole (QF) and defocusing quadrupole (QD) of a FODO cell are

$$\eta_{QF,x} = \frac{f_{QF}(4f_{QD}-L)\tilde{\phi}}{2f_{QF}+2f_{QD}-L},$$
$$\eta_{QD,x} = -\frac{f_{QD}(-4f_{QF}+L)\tilde{\phi}}{2f_{QF}+2f_{QD}-L}, \tag{A11}$$

where f_{QF} and f_{QD} are the focal lengths of QF and QD, respectively. $\tilde{\phi}$ is the dipole bending angle in each half FODO cell: $\tilde{\phi} = \pi/(PM)$. Note that with $L \ll R$, for small j,

$$\frac{1+a\gamma_0}{2\pi}\left[\frac{\eta_{QF,x}}{f_{QF}}\cos\left(j\frac{L}{R}\right)+\frac{\eta_{QD,x}}{f_{QD}}\right] \approx \frac{1+a\gamma_0}{PM}. \tag{A12}$$

For $j = 0$, the enhancement functions amount to PM so that $\xi_0 \approx -(1+a\gamma_0)$. Then, we consider $|\xi_j/\xi_0|$ with $|j| > 0$, i.e., the influence of the enhancement functions.

At ultrahigh beam energies, the total length of straight sections $PL_{\rm ss}$ only occupies a small fraction of the ring circumference $2\pi R$, since a high filling factor of dipoles is required to reduce the synchrotron-radiation energy loss. Taking the CEPC lattice as an example, the fraction is 0.18.

$\varsigma(P, \frac{j}{P})$ becomes P only for $j = kP, k \in \mathbb{Z}$, and is otherwise 0. In contrast, $|\varsigma[M, \frac{j}{MP}(1-\frac{PL_{\rm ss}}{2\pi R})]|$ approaches M when $\frac{j}{MP}(1-\frac{PL_{\rm ss}}{2\pi R})$ approaches an integer k but is less than $M/4$ when $|j| \geq P$ and $|j| < MP$. In addition, only a few k near the integer part of ν_0 have a significant influence in Eq. (34). The contribution of terms with very large $|j|$ is further suppressed by the $(\nu_0 - k + j)^2$ term in the denominator. Therefore, we can retain only ξ_0 in Eq. (34) as a reasonable approximation.

As an illustration, Fig. 13 shows the results of simulation for $|\xi_j/\xi_0|$ for various j, using the CEPC lattice. The CEPC lattice includes eight interleaved arc sections and straight sections. Each arc section contains 145 regular FODO cells and four FODO cells with half-bending angles as dispersion suppressors. In effect, $P = 8$ and $M = 149$. Then peaks of $|\xi_j/\xi_0|$ occur when j is near $kMP/(1-\frac{PL_{\rm ss}}{2\pi R})$, $k \in \mathbb{Z}$, agreeing with the observation in the Fig. 13(b). However, the eight straight sections have different functions and thus different lengths. There are also chromatic-correction sections with dipoles in the final focus systems. These are different from the model that we analyzed and somehow break the symmetry so that Fourier harmonics other than $j = 8k$ have comparable strengths, as shown in the Fig. 13(a). Nevertheless, the conclusion of our analysis still applies to the CEPC lattice, namely that the contribution of ξ_0 in Eq. (34) is much larger compared to other Fourier harmonics.

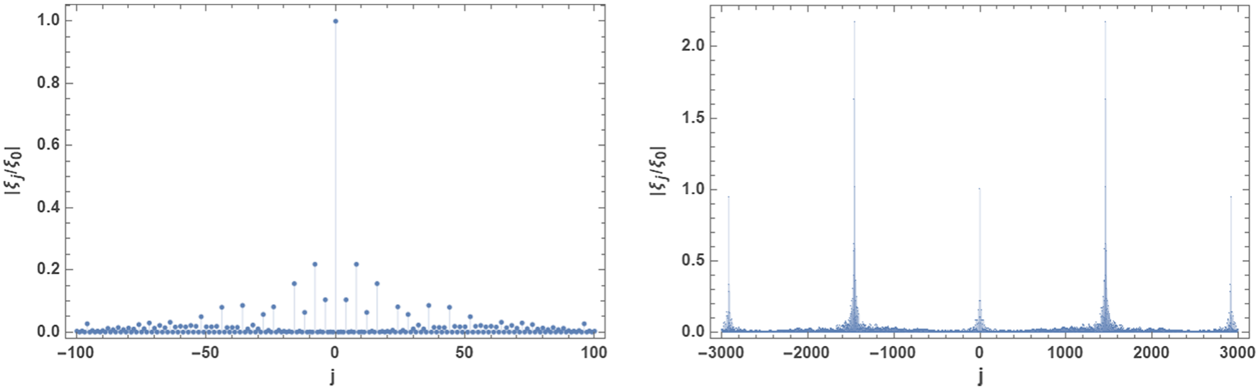

(a)

(b)

FIG. 13. $|\xi_j/\xi_0|$ for various j of the CEPC lattice at the Z pole. Peaks occur when j is near $kMP/(1-\frac{PL_{\rm SS}}{2\pi R})$, $k \in \mathbb{Z}$. (a) A smaller range $|j| < 100$. (b) A much larger range $|j| < 3000$.

3. More detailed theory of a double-frequency rf system

Our treatment of double rf systems follows the treatment in Chapter 3 of Ref. [74], but here and elsewhere we use a different convention for ϕ, whereby ϕ is the rf phase of a particle relative to that of the reference particle, rather than the phase coordinate ϕ_{Lee} relative to the fundamental rf system in Ref. [74]. Then $\phi = \phi_{\mathrm{Lee}} - \phi_{s1}$.

Then with time t as an independent variable, without considering radiation damping and quantum excitation, the equations of motion are

$$\begin{aligned} \frac{d\phi}{dt} &= h_1 \omega_0 \eta \delta \\ \frac{d\delta}{dt} &= \frac{e\omega_0}{2\pi E_0 \beta^2}\left[V_1 \sin(\phi + \phi_{s1}) + V_2 \sin(n\phi + \phi_{s2}) - \frac{U_0}{e}\right], \end{aligned} \tag{A13}$$

where $\omega_0 = c/R$, $\eta = \alpha_c - 1/\gamma_0^2$, α_c is the momentum compaction factor and h_1 is the harmonic number of the fundamental rf system. Equivalently, a particle's longitudinal motion is described by the Hamiltonian

$$\begin{aligned} H(\phi, \delta) &= \frac{h_1 \omega_0 \eta}{2}\delta^2 + \frac{e\omega_0}{2\pi E_0 \beta^2} U(\phi) \\ U(\phi) &= V_1 \cos(\phi + \phi_{s1}) + \frac{V_2}{n}\cos(n\phi + \phi_{s2}) \\ &\quad + \phi \frac{U_0}{e} - V_1 \cos(\phi_{s1}) - \frac{V_2}{n}\cos(\phi_{s2}). \end{aligned} \tag{A14}$$

This is a constant of motion for each particle and it is helpful to think of the term with δ^2 as being analogous to a kinetic energy, whereas the term with $U(\phi)$ can be thought of as a potential energy while the Hamiltonian is analogous to total energy.

To understand the synchrotron motion, one starts by solving for the fixed points, i.e., the solution of (ϕ, δ) such that

$$\begin{aligned} \frac{d\phi}{dt} &= 0, \\ \frac{d\delta}{dt} &= 0. \end{aligned} \tag{A15}$$

In our convention, we choose $(\phi, \delta) = (0, 0)$ as one such fixed point. Then the parameters of the double-frequency rf system must be set to compensate for the synchrotron-radiation energy loss per turn U_0, and this leads to Eq. (53). In the case of a single rf system, this is a stable fixed point around which small amplitude particles execute synchrotron oscillations. Besides, there is an unstable fixed point at $(\phi, \delta) = (\pi - 2\phi_{s1}, 0)$, which corresponds to the maximum value of the Hamiltonian, i.e., the boundary of the rf bucket.

In the case of a double rf system, the number and locations of the fixed points can be obtained by numerically solving Eq. (A15). In this paper, we focus on the cases with two fixed points, a stable fixed point at $(\phi, \delta) = (0, 0)$, and an unstable fixed point at $(\phi, \delta) = (\phi_{\mathrm{ufp}}, 0)$. The torus that passes through the unstable fixed point is called the separatrix. This separates phase space into regions of bound and unbound motions. We only study particle motion around the stable fixed point and within the boundary of the rf bucket enclosed by the separatrix, i.e., just the bound motion. Besides the unstable fixed point, there is another special point on the separatrix, $(\phi, \delta) = (\phi_{\mathrm{sep}}, 0)$, namely, the turning point at which the "kinetic energy" is zero and the "potential energy" is the "total energy." Since the beam energy range is well above the transition energy in this paper, i.e., $\eta > 0$, then $-\pi < \phi_{\mathrm{ufp}} < 0 < \phi_{\mathrm{sep}} < \pi$. Separatrices for cases A, B, and C with our settings are shown in Fig. 14 together with their unstable fixed points and their turning points. We see that for case C, the stable region in ϕ is indeed larger than in cases A and B. All three are mirror-symmetric across the ϕ axis.

Longitudinal phase-space trajectories of particles follow Hamiltonian torii $H(\phi, \delta) = H_0$, where H_0 is a constant of motion on a torus. The trajectories are also mirror symmetric across the ϕ axis. Then with Eq. (A14), an H_0 is the "potential energy" for the phase coordinates $\hat{\phi}_-$ and $\hat{\phi}_+$ with $(\phi_{\mathrm{ufp}} < \hat{\phi}_- < 0 < \hat{\phi}_+ < \phi_{\mathrm{sep}})$ at which "kinetic energy" is zero, namely at $\delta = 0$. On the other hand, the maximum "kinetic energy" written as $h_1 \omega_0 \eta \hat{\delta}^2/2$ occurs at the minimum of the "potential energy," namely, at $\phi = 0$ where $U(\phi) = 0$. Then

$$H_0 = \frac{h_1 \omega_0 \eta}{2}\hat{\delta}^2 = \frac{e\omega_0}{2\pi E_b \beta^2} U(\hat{\phi}_-) = \frac{e\omega_0}{2\pi E_b \beta^2} U(\hat{\phi}_+) \tag{A16}$$

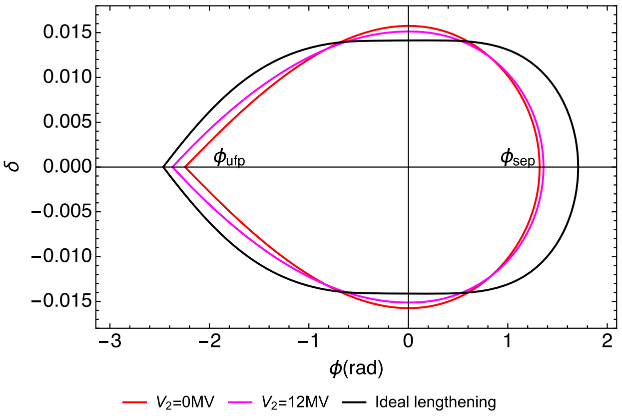

FIG. 14. The separatrices for various settings of a double rf system. The locations of ϕ_{ufp} and ϕ_{sep} are also labeled. The red curve corresponds to case A with a single rf system alone, the magenta curve corresponds to one instance of case B with $\phi_{s2} = 0$ rad but $V_2 = 12$ MV, the black curve corresponds to case C at the ideal lengthening condition.

so that H_0 expresses the amplitude of the synchrotron motion in terms of $\hat{\delta}$, $\hat{\phi}_-$, or $\hat{\phi}_+$.

Equation (A14) can be written as

$$\frac{h_1\omega_0\eta}{2}\delta^2 = H_0 - \frac{e\omega_0}{2\pi E_0\beta^2}U(\phi).$$

Then the synchrotron oscillation period can be obtained by using this to integrate the first equation of Eq. (A13):

$$T_z = \oint d\phi\left(2h_1\omega_0\eta\left[H_0 - \frac{e\omega_0}{2\pi E_0\beta^2}U(\phi)\right]\right)^{-1/2}. \tag{A17}$$

This can be numerically evaluated for a specified H_0 so that we can then obtain the synchrotron tunes, $\nu_z = \frac{2\pi}{T_z\omega_0}$, plotted in Fig. 9(a). For each H_0, a measure of the maximum longitudinal distance of a particle from the center of the bunch is $z_{H_0} \equiv \frac{(\hat{\phi}_+ - \hat{\phi}_-)R}{2h_1}$ and this, being more recognizable, is used instead of H_0 as the horizontal axis in Fig. 9(a).

In the presence of radiation damping and quantum excitation, the longitudinal phase-space distribution settles to an equilibrium given by the static solution of the Fokker-Planck equation [78], namely, $\tilde{\psi}(\delta,\phi) \propto \exp[-\text{constant}\times H(\phi,\delta)]$. This distribution is approximately Gaussian in δ with an rms relative energy spread σ_δ, while the distribution of ϕ is

$$\tilde{\rho}(\phi) = A_\rho \exp\left(-\frac{eU(\phi)}{2\pi E_0 h_1\eta\sigma_\delta^2}\right), \tag{A18}$$

where A_ρ is a normalization factor chosen so that $\int_{\phi_{\text{ufp}}}^{\phi_{\text{sep}}}\tilde{\rho}(\phi)d\phi = 1$. The first-order and second-order beam moments can be numerically evaluated by

$$\begin{aligned}\bar{\phi} &= \int_{\phi_{\text{ufp}}}^{\phi_{\text{sep}}}\phi\tilde{\rho}(\phi)d\phi \\ \Sigma_\phi &= \int_{\phi_{\text{ufp}}}^{\phi_{\text{sep}}}(\phi-\bar{\phi})^2\tilde{\rho}(\phi)d\phi.\end{aligned} \tag{A19}$$

The longitudinal distributions, $\tilde{\rho}(\phi)$, are shown in Fig. 9(b) and are obtained by numerically evaluating the rhs of Eq. (A18). The horizontal axis in Fig. 9(b) is the longitudinal coordinate $z = -\beta c\Delta t = \frac{\phi R}{h_1}$. The rms bunch length is then

$$\sigma_z = \frac{\sqrt{\Sigma_\phi}R}{h_1}. \tag{A20}$$

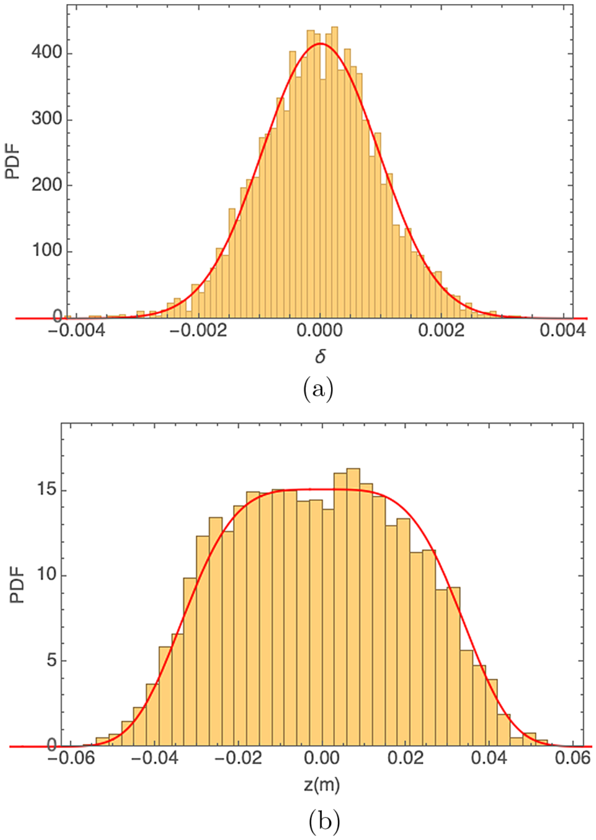

(a)

(b)

FIG. 15. The longitudinal beam distributions of case C at the ideal lengthening condition. The red curves are the theoretical probability density function (PDF), and the histograms are obtained from the final beam distribution of a Monte Carlo simulation, where 4000 particles are tracked for 10 damping times (about 25 000 turns). The beam energy is set to 45.72 GeV ($a\gamma_0 = 103.76$) and $V_1 = 103.372$ MV. (a) Distribution of relative energy deviation δ. (b) Distribution of relative longitudinal positron z.

Note that the second-order beam moments at equilibrium are usually calculated using the beam-envelope matrix as in [79]. That method is still applicable for the calculation of the rms energy spread, but it fails to deliver the correct rms bunch length in the presence of a double rf system, because $U(\phi)$ now contains components higher than second order in ϕ, which are not properly taken into account by that method. In this case, one can use Eqs. (A19) and (A20) to numerically evaluate σ_z, or use Monte Carlo simulation to obtain σ_z.

In any case, Fig. 15 shows the probability density functions (PDF) of the beam distributions in δ and z, for case C at the ideal lengthening condition, where the theoretical distributions match well with the histograms from the final beam distribution of a Monte Carlo simulation with localized cavities and full synchrobetatron motion tracking with 4000 particles for ten damping times (about 25 000 turns). The beam energy is set to 45.72 GeV ($a\gamma_0 = 103.76$) and $V_1 = 103.372$ MV.

---

[1] A. Abada *et al.*, FCC-ee: The lepton collider, Eur. Phys. J. Spec. Top. **228**, 261 (2019).

[2] V. Shiltsev and F. Zimmermann, Modern and future colliders, Rev. Mod. Phys. **93**, 015006 (2021).

[3] The CEPC Study Group, CEPC conceptual design report volume I-accelerator, arXiv:1809.00285.

[4] CEPC Accelerator Study Group, Snowmass2021 White Paper AF3-CEPC (2022), arXiv:2203.09451.

[5] Y. S. Derbenev *et al.*, Accurate calibration of the beam energy in a storage ring based on measurement of spin precession frequency of polarized particles, Part. Accel. **10**, 177 (1980), https://inspirehep.net/literature/159462.

[6] R. W. Assmann *et al.*, Calibration of centre-of-mass energies at LEP1 for precise measurements of Z properties, Eur. Phys. J. C **6**, 187 (1998).

[7] Z. Duan *et al.*, Concepts of longitudinally polarized electron and positron colliding beams in the Circular Electron Positron Collider, in *Proceedings of IPAC2019, Melbourne, Australia* (JACoW, Geneva, Switzerland, 2019), paper MOPMP012.

[8] W. H. Xia *et al.*, Investigation of spin rotators in CEPC at the Z-pole, Radiat. Detect. Technol. Methods **6**, 490 (2022).

[9] T. Chen, Z. Duan, D. Ji, and D. Wang, Booster free from spin resonance for future 100-km-scale circular e^+ e^- colliders, Phys. Rev. Accel. Beams **26**, 051003 (2023).

[10] L H Thomas, The kinematics of an electron with an axis, Philos. Mag. **3**, 1 (1964).

[11] V. Bargmann, L. Michel, and V. L. Telegdi, Precession of the Polarization of Particles Moving in a Homogeneous Electromagnetic Field, Phys. Rev. Lett. **2**, 435 (1959).

[12] D. P. Barber, J. Ellison, and K. Heinemann, Quasiperiodic spin-orbit motion and spin tunes in storage rings, Phys. Rev. ST Accel. Beams **7**, 124002 (2004).

[13] G. H. Hoffstaetter, H. S. Dumas, and J. A. Ellision, Adiabatic invariance of spin-orbit motion in accelerators, Phys. Rev. ST Accel. Beams **9**, 014001 (2006).

[14] A. W. Chao, Evaluation of beam distribution parameters in an electron storage ring, J. Appl. Phys. **50**, 595 (1979).

[15] V. N. Baier, V. M. Katkov, and V. M. Strakhovenko, Kinetics of radiative polarization, Sov. Phys. JETP **31**, 908 (1970), http://www.jetp.ras.ru/cgi-bin/dn/e_031_05_0908.pdf.

[16] Y. S. Derbenev and A. M. Kondratenko, Polarization kinematics of particles in storage rings, Sov. Phys. JETP **37**, 968 (1973), https://wiki.jlab.org/ciswiki/images/4/4b/E_037_06_0968.pdf.

[17] S. Mane, Electron-spin polarization in high-energy storage rings. I. Derivation of the equilibrium polarization, Phys. Rev. A **36**, 105 (1987).

[18] V. N. Baier and Y. F. Orlov, Quantum depolarization of electrons in a magnetic field, Sov. Phys. Dokl. **10**, 1145 (1966), https://inspirehep.net/literature/48627.

[19] Y. S. Derbenev, A. M. Kondratenko, and A. N. Skrinsky, Radiative polarization at ultra-high energies, Part. Accel. **9**, 247 (1979), https://inspirehep.net/literature/146068.

[20] A. M. Kondratenko, The stability of the polarization of colliding beams, Sov. Phys. JETP **39**, 592 (1974), http://jetp.ras.ru/cgi-bin/dn/e_039_04_0592.pdf.

[21] Y. S. Derbenev and A. M. Kondratenko, Relaxation of the equilibrium state of polarization of electrons in storage rings, Sov. Phys. Dokl. **19**, 438 (1975).

[22] D. P. Barber and G. Ripken, Section 2.7.8, computing algorithms and spin matching, in *Handbook of Accelerator Physics and Engineering*, edited by A. W. Chao *et al.*, (World Scientific, Singapore, 2006), 1st ed., 3rd printing.

[23] D. P. Barber and G. Ripken, Section 2.6.7, computing algorithms for e^-/e^+ polarization in storage rings, in *Handbook of Accelerator Physics and Engineering*, edited by A. W. Chao *et al.* (World Scientific, Singapore, 2023), 3rd ed.

[24] A. Chao, Evaluation of radiative spin polarization in an electron storage ring, Nucl. Instrum. Methods **180**, 29 (1981).

[25] S. R. Mane, Electron-spin polarization in high-energy storage rings. II. Evaluation of the equilibrium polarization, Phys. Rev. A **36**, 120 (1987).

[26] K. Yokoya, Nonperturbative calculation of equilibrium polarization of stored electron beams, KEK Report No. KEK-92-6, 1992.

[27] K. Yokoya, An algorithm for calculating the spin tune in circular accelerators, DESY Report No. 99-006, 1999.

[28] K. Yokoya, Calculation of the equilibrium polarization of stored electron beams using Lie Algebra, Nucl. Instrum. Methods Phys. Res., Sect. A **258**, 149 (1987).

[29] J. Kewisch, Ph.D. thesis, Hamburg University, 1985.

[30] D. P. Barber, Polarization in the eRHIC electron (positron) ring, in *Proceedings of Spin 2004* (World Scientific, Trieste, Italy, 2005), pp. 738–741.

[31] D. Sagan, Bmad: A relativistic charged particle simulation library, Nucl. Instrum. Methods Phys. Res., Sect. A **558**, 356 (2006).

[32] D. Sagan, The Bmad Reference Manual, https://www.classe.cornell.edu/bmad/manual.html.

[33] R. Assmann *et al.*, Spin dynamics in LEP with 40–100 GeV beams, AIP Conf. Proc. **570**, 169 (2001).

[34] S. R. Mane, Polarization at TLEP/FCC-ee: Ideas and estimates, arXiv:1406.0561.

[35] S. A. Nikitin, Opportunities to obtain polarization at CEPC, Int. J. Mod. Phys. A **34**, 1940004 (2019).

[36] S. A. Nikitin, Polarization issues in circular electron–positron super-colliders, Int. J. Mod. Phys. A **35**, 2041001 (2020).

[37] K. Heinemann, D. Appelö, D. P. Barber, O. Beznosov, and J. A. Ellison, The Bloch equation for spin dynamics in electron storage rings: Computational and theoretical aspects, Int. J. Mod. Phys. A **34**, 1942032 (2019).

[38] B. Oleksii, From wave propagation to spin dynamics: Mathematical and computational aspects, Ph.D. thesis, University of New Mexico, 2020.

[39] K. Heinemann, D. Appelö, D. P. Barber, O. Beznosov, and J. A. Ellison, Int. J. Mod. Phys. A **35**, 2041003 (2020).

[40] E. Gianfelice-Wendt, Phys. Rev. Accel. Beams **19**, 101005 (2016).

[41] I. A. Koop, Resonant depolarization at Z and W at FCC-ee, *Proceedings of eeFACT 2018* (2018), paper TUPBB04, pp. 165–168.

[42] E. Forest, F. Schmidt, and E. McIntosh, Introduction to the polymorphic tracking code, CERN and KEK Report No. CERN-SL-2002-044 (AP), and KEK-Report 2002-3, 2002, https://frs.web.cern.ch/frs/report/sl-2002-044.pdf.

[43] E. Forest, FPP Manual, https://usermanual.wiki/Document/fppmanual.653439610/help.

[44] Z. Duan, M. Bai, D. P. Barber, and Q. Qin, A Monte-Carlo simulation of the equilibrium beam polarization in ultra-high energy electron (positron) storage rings, Nucl. Instrum. Methods Phys. Res., Sect. A **793**, 81 (2015).

[45] K. Yokoya, Spin chromaticity for higher-order synchrotron resonances, Part. Accel. **13**, 85 (1983), https://inspirehep.net/literature/182602.

[46] K. Yokoya, Beam polarization in high energy electron storage rings, KEK Report 85-7, 1986.

[47] G. H. Hoffstaetter, *High-Energy Polarized Proton Beams: A Modern View*, Springer Tracts in Modern Physics Vol. 218 (Springer, New York, NY, 2006).

[48] G. H. Hoffstatter, M. Vogt, and D. P. Barber, Higher order effects in polarized proton dynamics, Phys. Rev. ST Accel. Beams **2**, 114001 (1999).

[49] M. Vogt, Bounds on the maximum attainable equilibrium spin polarization of protons at high energy in HERA, Ph.D. thesis, University of Hamburg, 2000.

[50] S. Y. Lee, *Spin Dynamics and Snakes in Synchrotrons* (World Scientific, Singapore, 1997).

[51] Note, however, that the Eq. 3.3 in Ref. [19] suffers from an error whereby the exponent in the denominator should be 4 instead of 2.

[52] A. M. Kondratenko, Radiative polarization in storage rings, BINP Report No. 82-28, 1982.

[53] B. Montague, Polarized beams in high energy storage rings, Phys. Rep. **113**, 1 (1984).

[54] R. Rossmanith and R. Schmidt, Compensation of depolarizing effects in electron-positron storage rings, Nucl. Instrum. Methods Phys. Res., Sect. A **236**, 231 (1985).

[55] D. Barber *et al.*, High spin polarization at the HERA Electron Storage Ring, Nucl. Instrum. Methods Phys. Res., Sect. A **338**, 166 (1994).

[56] R. Assmann, A. Blondel, B. Dehning *et al.*, Lepton beam polarization at LEP, AIP Conf. Proc. **343**, 219 (1995).

[57] S. R. Mane, Synchrotron sideband spin resonances in high-energy electron storage rings, Nucl. Instrum. Methods Phys. Res., Sect. A **292**, 52 (1990).

[58] S. R. Mane, Polarization of electron beams in high energy storage rings Part I. Convergence of perturbation theory, Nucl. Instrum. Methods Phys. Res., Sect. A **321**, 21 (1992).

[59] S. R. Mane, Polarization of electron beams in high energy storage rings. Part II. Series expansion with tune modulation, Nucl. Instrum. Methods Phys. Res., Sect. A **321**, 42 (1992).

[60] B. Wang *et al.*, A correction scheme for the magnet imperfection on the CEPC Collider Ring, in *Proceedings of IPAC2021*, (JACoW, Geneva, Switzerland, 2021), paper TUPAB007, p. 1346.

[61] SAD home page, https://acc-physics.kek.jp/SAD/.

[62] A. Terebilo, Accelerator toolbox for MATLAB, SLAC Report No. SLAC-PUB-8732, 2001.

[63] D. Zhou *et al.*, Lattice translation between accelerator simulation codes for SuperKEKB, in *Proceedings of IPAC2016, Busan, Korea* (JACoW, Geneva, Switzerland, 2016), paper WEPOY040.

[64] A. Blondel and J. M. Jowett, Wigglers for polarization, Conf. Proc. C **8711093**, 216 (1987), https://cds.cern.ch/record/369485/files/216.pdf.

[65] W. Xia, J. Gao, Y. Wang, and D. Wang, CEPC Z-pole polarization design studies, Int. J. Mod. Phys. A **36**, 2142003 (2021).

[66] M. Sands, The physics of electron storage rings an introduction, SLAC Report No. 121, 1970.

[67] K. Ohmi, N. Kuroo, K. Oide, D. Zhou, and F. Zimmermann, Coherent Beam-Beam Instability in Collisions with a Large Crossing Angle, Phys. Rev. Lett. **119**, 134801 (2017).

[68] N. Kuroo, K. Ohmi, K. Oide, D. Zhou, and F. Zimmermann, Cross-wake force and correlated head-tail instability in beam-beam collisions with a large crossing angle, Phys. Rev. Accel. Beams **21**, 031002 (2018).

[69] Y. Zhang, N. Wang, C. Lin, D. Wang, C. Yu, K. Ohmi, and M. Zobov, Self-consistent simulations of beam-beam interaction in future e^+e^- circular colliders including beamstrahlung and longitudinal coupling impedance, Phys. Rev. Accel. Beams **23**, 104402 (2020).

[70] C. Lin, K. Ohmi, and Y. Zhang, Coupling effects of beam-beam interaction and longitudinal impedance, Phys. Rev. Accel. Beams **25**, 011001 (2022).

[71] M. Migliorati, E. Carideo, D. de Arcangelis, Y. Zhang, and M. Zobov, Eur. Phys. J. Plus **136**, 1190 (2021).

[72] P. Raimondi, Updates on monochromatization, in *Proceedings of FCC-FS EPOL Group and FCCIS WP2.5 Meeting 15* (2022); D. Shatilov and P. Raimondi, FCC-ee parameters and challenges, in *Proceedings of FCCIS Workshop* (2022).

[73] A. Hofmann and S. Myers, Beam dynamics in a double RF system, Experientia **40**, 610 (1980).

[74] S. Y. Lee, *Accelerator Physics* (World Scientific, Hackensack, NJ, 2004), 2nd ed.

[75] Y. S. Derbenev and A. M. Kondratenko, Diffusion of particle spin in storage rings, Sov. Phys. JETP **35**, 230 (1972), http://jetp.ras.ru/cgi-bin/dn/e_035_02_0230.pdf.

[76] P. Nishikawa, D. Sagan, and G. H. Hoffstaetter, Using Taylor Maps with Synchrotron Radiation Effects Included, in *Proceedings of IPAC 2022* (JACoW, Geneva, Switzerland, 2022), paper WEPOMS053, p. 2376.

[77] A. Blondel *et al.*, Polarization and centre-of-mass energy calibration at FCC-ee, arXiv:1909.12245.

[78] J. M. Jowett, Introductory statistical mechanics for electron storage rings, AIP Conf. Proc. **153**, 864 (1987).

[79] K. Ohmi, K. Hirata, and K. Oide, From the beam-envelope matrix to synchrotron-radiation integrals, Phys. Rev. E **49**, 751 (1994).